J. Fluid Mech. (2002), *vol.* 472, *pp.* 167–200.
DOI: 10.1017/S0022112002002264 Printed in the United Kingdom

The evolution of round zero-net-mass-flux jets

By JOHN E. CATER AND JULIO SORIA

Laboratory for Turbulence Research in Aeronautics and Combustion, Department of Mechanical Engineering, Monash University, Melbourne, VIC 3800, Australia

(Received 19 October 2001 and in revised form 30 June 2002)

This paper reports on an experimental investigation to determine the structure and mean flow quantities of round zero-net-mass-flux (ZNMF) jets. These jets are generated by a piston oscillating in a cavity behind a circular orifice. Several different flow patterns were observed with dye flow visualization and a parameter map of these was generated. Cross-correlation digital particle image velocimetry was used to measure instantaneous two-dimensional in-plane velocity fields in a plane containing the orifice axis. These velocity fields are used to investigate the existence of a self-preserving velocity profile in the far field of the ZNMF jet. The mean flow quantities and turbulent statistics of the ZNMF jets were compared with measurements for 'equivalent' continuous jets in the same apparatus. Phase-averaged velocity measurements were obtained in the near field of the ZNMF jets and were used to determine the radial entrainment. The out-of-plane vorticity fields were also investigated to gain an understanding of the mechanisms responsible for the difference in spreading rate of ZNMF jets compared to conventional continuous jets. A conceptual model of the ZNMF jet structure in the near field for Strouhal numbers much less than one is proposed that explains the observed behaviour of these ZNMF jets.

1. Introduction

In an overview of acoustic streaming Lighthill (1978) summarizes the two methods for generating fluid streams. The first is the transmission of pressure waves through a compressible medium. The second, which is the focus of the present study, is the streaming motions that can be generated by viscous effects at a boundary. A zero-net-mass-flux (ZNMF) jet is a fluid stream with non-zero mean streamwise momentum formed by the interaction of vortices. The vortices are generated by the periodic oscillation of a fluid boundary and propagate due to the nonlinear term in the equations of motion. The vortices are created within the fluid in which the generator is deployed without the net injection of additional fluid. This feature makes ZNMF jets attractive for applications in fluid mixing where the cost, bulk and mixing efficiency of the mechanism is a primary consideration.

The mixing properties of mechanically excited fluid streams has been previously studied by examining the behaviour of pulsing jet flows. These jets consist of periodic flow oscillations superimposed on a mean continuous stream. Pulsed jets are classified by the velocity amplitude of the imposed forcing. When the RMS velocity is small ($< 10\%$ of the mean velocity), the forcing is said to be 'low amplitude'. Above this threshold the forcing is considered to be 'high amplitude' up to the condition where the amplitude of the excitations produces a maximum velocity at the jet centreline with a magnitude equal to the mean velocity of the jet across the exit plane. This flow is termed a 'fully pulsed' jet. A comparison of fully pulsed jets was performed

in the experimental work of Bremhorst & Hollis (1990). The ZNMF jet (also called a synthetic jet) is considered to be a special case of the fully pulsed jet flow, since the mean velocity is zero and it is generated wholly by a pulsing action. However, the fundamental difference in the fluid mechanics between a ZNMF jet and a fully pulsed jet during formation is the period when the flow direction at the generator is reversed.

The number of applications for ZNMF jets as flow actuators has increased considerably since the discovery that they can be manufactured at micron scales using micro-piezoelectric manufacturing technology. A ZNMF jet generated by a round piezoelectric device was investigated in James, Jacobs & Glezer (1996). In this study a jet was produced by a piezoelectric diaphragm mounted flush with a wall and submerged in water. However, a ZNMF jet was only generated for high amplitudes of oscillation when cavitation bubbles formed at the diaphragm surface. The formation of the jet was therefore attributed to the motions caused by the periodic formation and collapse of the bubbles. The spreading of the resultant jet was less than that of a conventional jets at a similar source Reynolds number, but mean profiles were found to be self-similar within the measurement resolution of the apparatus. It was noted that an array of ZNMF jet flow actuators mounted on a surface permits the dynamic changing of a flow boundary condition.

In Smith & Glezer (1997) it was shown that jet formation can be enhanced under most circumstances by using a cavity partially closed by an orifice and fitted with an internal oscillator. It was also shown that the behaviour of shear flows can be manipulated by pairs of ZNMF jets placed on either side of a jet. By oscillating the ZNMF jets at frequencies an order of magnitude higher than the unstable frequencies in a shear layer, a nonlinear amplification of disturbances was produced. These disturbances can effect changes that are one or two orders of magnitude greater than the dominant length scale of the flow. The vectoring of shear flows manipulated in this way is accompanied by an increase in fine-scale motions in the flow, which provides further opportunities for the application of ZNMF jets to the enhancement of mixing in fluids.

The mean properties of plane (or rectangular) jets were investigated by Smith & Glezer (1998) and compared to the properties of conventional two-dimensional jets. At each oscillation of the actuator within the rectangular cavity, the flow separates at the orifice edge and coalesces to form the mean jet flow. The jet flows were generated at a fixed frequency for a source Reynolds number of 383, based on the peak axial velocity at the orifice. The vortices produced were initially laminar at this relatively low Reynolds number. The transition of the jet to turbulence was attributed to the breakdown of the vortices due to a wavy spanwise instability. This appears to be equivalent to the inviscid azimuthal instability in the breakup of vortex rings as observed in Widnall & Tsai (1977). In that study, hot-wire probes were used to investigate the evolution of the centreline velocity and the results showed a rate of decay typical of a plane jet.

ZNMF jets were investigated numerically by Kral *et al.* (1997). They studied the behaviour of two-dimensional laminar and turbulent ZNMF jets and compared them to steady and fully pulsed jets. The flows were classified using the time-averaged momentum flow of the jets over half the period. The flow within the generation cavity was not computed; instead a simple harmonic oscillatory velocity boundary condition was employed to model the flow at the orifice. A number of orifice velocity distributions were investigated including the 'top-hat' profile. At low source Reynolds

numbers the computed flow structure was identified from the vorticity fields to be a series of laminar vortex pairs. The mean velocity profiles were only qualitatively in agreement with the experimental results of Smith & Glezer (1997) in the near-field region. However, the agreement became more satisfactory at large distances from the orifice. No comparison of the fluctuating components of the velocity field was presented.

Rizzetta, Visbal & Stanek (1999) extended the domain of ZNMF jet simulations to three dimensions in an attempt to match more closely the physics of the fluid mechanism responsible for the breakup of jets in the experiments of Smith & Glezer (1997). However, resource limitations prevented the simulation of rectangular jets with the same aspect ratio. This work also simulated the cavity flow for two different cavity depths, in an attempt to explain the differences between the experimental studies and the results of Kral *et al.* (1997). The driving boundary was simulated by a sinusoidal inflow, but the resultant motion through the orifice was found to be non-similar in time. This was attributed to the formation of regions of vorticity within the cavity. Laminar simulations produced a series of laminar rings without the formation of a continuous stream. The single turbulent case modelled in that study showed poor agreement with experimental velocity measurements.

Multiple micro-scale ZNMF jets have also been used to enhance the mixing properties of continuous jets. For example, Davis & Glezer (1999) used a series of ZNMF jet actuators placed in a concentric ring around a circular orifice to stimulate fine-scale structures within the shear layer of a round jet. These actuators were manipulated to excite the jet flow in two modes, axially or radially. By varying the amplitude of oscillation, it was discovered that instabilities in the shear layer could be suppressed or amplified. It was also shown that excitation of the jet results in increased jet dispersion and increases the total entrainment.

In the present work a ZNMF jet that is axisymmetric in the mean is formed from the interaction of vortex rings that separate at a round orifice. The flow through the orifice is produced by the periodic oscillation of a piston within a cylindrical cavity. A study was undertaken to identify the flow structure in the developing region of the ZNMF jet that govern the dynamics of the flow. The in-plane velocity fields and temporal velocity gradients were measured to determine the functional dependence of the mean velocity profiles and second-order turbulence statistics on axial displacement in the flow development region.

2. Flow parameterization

2.1. *Characteristic scales and non-dimensionalization*

The dimensionless groups that have been identified to characterize the ZNMF jet flow field are the source Reynolds number and the Strouhal number. To non-dimensionalize the flow field using these parameters it is necessary to determine appropriate length, velocity and time scales for the flow. From the flow generation apparatus an obvious choice for a length scale is D_0, the orifice diameter. This scale is used in both the source Reynolds number and the Strouhal number to classify the global flow pattern and behaviour. The source Reynolds number is

$$Re_0 = \frac{U_0 D_0}{\nu}, \tag{2.1}$$

where U_0 is a characteristic velocity scale. The Strouhal number based upon the frequency of oscillation f, and the same velocity and length scales is

$$St_0 = \frac{fD_0}{U_0}. \tag{2.2}$$

In previous work on continuous jets the mean velocity across the orifice or the peak centreline velocity has often been chosen as the characteristic velocity scale. The choice of a characteristic velocity scale is less obvious for a ZNMF jet since the integrated mean exit velocity of the fluid through the orifice is zero. In the studies of pulsed jets in cross-flow, the jets have been characterized by the mean velocity (Chang & Vakili 1995; Hermanson, Wahba & Johari 1998; Johari, Pacheco-Tougas & Hermanson 1999; Vermeulen, Chin & Yu 1990; Wu, Vakili & Yu 1988) or the mean momentum of each pulse (Eroglu & Breidenthal 2001). Studies of ZNMF jets use either a mean velocity over the injection half of the cycle (Smith & Glezer 1998), or the maximum jet velocity (Kral *et al.* 1997), or a mean jet velocity at some distance from the orifice (Mallinson, Hong & Reizes 1999; Rizzetta *et al.* 1999).

A more appropriate velocity scale at the jet source can be derived by examining the flow at the orifice exit plane. If it is assumed that the flow generation mechanism (in this case the piston) has a constant mean position, then no net mass is injected. However, there is a net momentum flow through the exit plane, and energy is transferred to the environment. This suggests that a velocity scale based on mean momentum flow should be considered. If the mean-squared integral of the velocity profile over an oscillation period is calculated, a non-zero quantity results. Dividing the resulting mean momentum flow by the orifice area followed by taking the square root results in a quantity which has the units of velocity (or average specific momentum). This characteristic velocity is termed the *momentum flow velocity* and is given by

$$U_0 = \left[\frac{4}{\pi D_0^2 T_0} \int_0^{T_0} \int_0^{D_0/2} 2\pi r u(r,t) u(r,t) \, \mathrm{d}r \, \mathrm{d}t \right]^{1/2}. \tag{2.3}$$

The streamwise coordinate is x and the radial coordinate is r, both of which are measured from the orifice centreline. The azimuthal direction is perpendicular to both x and r and is denoted by θ. The oscillation period is T_0. For the continuous jet the same analysis results in the mean mass flow velocity across the orifice. ZNMF and continuous jets are matched throughout the present work by equating the momentum flow velocity. For a sinusoidal excitation the ZNMF jet has a peak exit velocity at the orifice that is $\sqrt{2}$ larger than the mean velocity of the equivalent continuous jet, assuming that the orifice velocity profiles have the same shape.

The Reynolds number of the ZNMF jet can be systematically manipulated by changing the frequency of oscillation and thus changing the momentum flow velocity at the orifice. The other parameter that can be varied is the amplitude of the oscillation. In this study the relative amplitude of the oscillations is large compared to the orifice size such that the length of the ejected slug of fluid non-dimensionalized by the orifice diameter is approximately 30. Increasing the amplitude of the excitations has the effect of increasing the Reynolds number and decreasing the Strouhal number. Thus, if the streamwise profile of the flow through the orifice is solely a function of Reynolds number, the Strouhal number is essentially the inverse of a non-dimensional oscillation amplitude.

2.2. *Self-preservation of the jet flow*

The possibility of self-preserving solutions to the governing equations of axisymmetric jets has long been recognized, as noted in Tennekes & Lumley (1972). Usually, solutions to the steady axisymmetric equations are sought in terms of a similarity variable which is the radial coordinate non-dimensionalized by the axial location, $\eta = r/(x - x_0)$. A velocity virtual origin (x_0) is also included to simulate a point source of momentum for the jet.

Dimensional analysis of the far field using the principle of conservation of momentum leads us to expect a linear growth of the jet at a rate that depends on the source Reynolds number and a decrease of the centreline velocity with x^{-1} such that for a self-preserving jet the relationship for the centreline velocity becomes

$$\frac{U_0}{U_c} = S_u \left(\frac{x - x_0}{D_0} \right). \tag{2.4}$$

S_u is a constant that depends on the experimental facility and is known as the 'decay constant'. This expression can be re-written in terms of the jet momentum M_j:

$$U_c = B \left(\frac{M_j^{1/2}}{x - x_0} \right), \tag{2.5}$$

where $B = 2/(\sqrt{\pi} S_u)$. Often, a second virtual origin x_s is included in the analysis of the jet spread, so that the growth of the jet half-width $r_{1/2}$, is given by $r_{1/2} = S_b(x - x_s)$. S_b is known as the 'spreading rate'. For a top-hat profile, an analytical model of a jet in an infinite environment gives the values for these constants as $S_u = 0.1695$ and $S_b = 0.1$. Although these scaling relationships have been found to be non-universal by George (1989), this approach is useful for comparison with other published data. The actual structure of the jet flow is discussed in § 6.1.

3. Experimental technique

3.1. *Flow geometry*

The experimental measurements of the ZNMF and continuous jets were carried out in an acrylic tank 1000 mm long, 500 mm wide and 500 mm deep, filled with filtered water. To remove the air/water interface within the facility, the tank has a riser tube with an inner diameter of 56.5 mm located on the Perspex roof at the far end of the tank from the piston normal to the jet axis, and the facility was filled with water to the Perspex roof. The riser tube removes the net mass injected during the continuous jet experiments.

In each experiment jets were formed by discharging water from a circular cylinder of inner diameter $D_p = 50$ mm through an orifice plate of diameter $D_0 = 2$ mm, positioned in the centre of the endwall of the tank using a piston in the cylindrical cavity. The dimensionless groups that characterize the geometry of the apparatus are: a contraction ratio, a dimensionless cavity depth and a slug length. These are given by $A_R = D_p^2/D_0^2$, $C_0 = \overline{C}/D_p$ and $L_D = L_p A_R/D_0$, respectively, where $\overline{C}$ is the mean depth of the cavity and L_p is the stroke length of the piston.

The contraction ratio of the apparatus between the cavity and the orifice was held constant at $A_R = 625$. The thickness of the orifice plate is the same as the diameter of the opening, so that the generator matches the geometry simulated in Rizzetta *et al.* (1999). The detailed geometric arrangement is shown in figure 1. Two different orifice

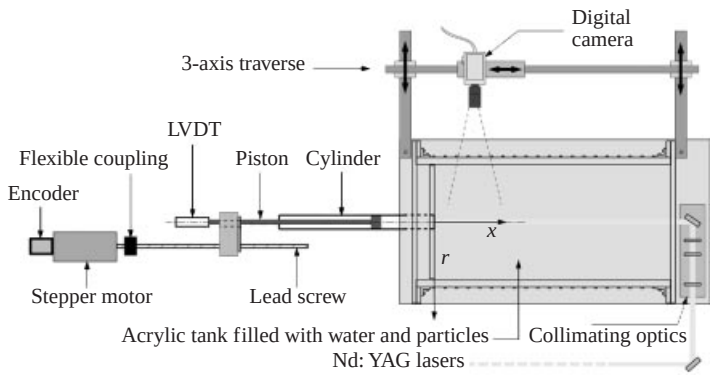

FIGURE 1. Schematic of jet generation apparatus. The internal dimensions of the tank are $500 \times 500 \times 1000$ mm. The tank is filled with water, at a temperature of 19 °C, initially at rest. Orifice plates are attached to the end of the piston cylinder and mounted with the external surface flush with a false wall inside the tank.

plates were used in this work, each was manufactured with a thickness of 2 mm, but with different inner edge geometries. For the flow visualization experiments, a blunt-edged orifice was chosen. This was later abandoned for the particle image velocimetry (PIV) velocity measurements due to concerns about the effect of flow separation from the inner edge of the orifice during the forward stroke as seen in the computed results of Rizzetta *et al.* (1999). To preserve flow symmetry at the orifice during the forward and reverse strokes, the blunt-edged orifice plate was replaced for the remaining measurements with a orifice plate bevelled at 45° on both faces. Comparative flow visualization conducted using both orifice plates did not reveal any differences in the behaviour of the jets.

Continuous jets were generated by a long, constant-velocity stroke of the piston. At the end of each experiment the finishing position of the piston was $50D_0$ from the orifice, inside the cavity. The orifice plate obscured the optical path at the generator so that the flow behind the orifice could not be measured or easily visualized in this facility.

The generating mechanism for the ZNMF jets consisted of the same piston/cylinder arrangement used to generate the continuous jet with the stepper motor programmed to oscillate with a time-periodic function that approximates a sine curve. The mean position of the piston during the generation of ZNMF jet flows was maintained at $50D_0$ from the external face of the orifice plate within the cavity, which gives a constant non-dimensional cavity depth of $C_0 = 1.0$.

The dimensions of the experimental facility are a concern, particularly for the continuous jets because the bounded nature of the facility necessitates a reversed flow outside the jets. The loss of momentum of the jets due to the reverse flow can be estimated following the technique outlined by Hussein, Capp & George (1994). If it is assumed that the return flow around the jet U_R is constant, that mass is conserved and the viscous effects at the walls are neglected, the equation for the momentum flow in a streamwise plane is

$$M = \int_{jet} u^2 \, \mathrm{d}A + \int_{reverse} U_R^2 \, \mathrm{d}A. \tag{3.1}$$

If we further assume that the area covered by the jet flow is small and we set A_R to

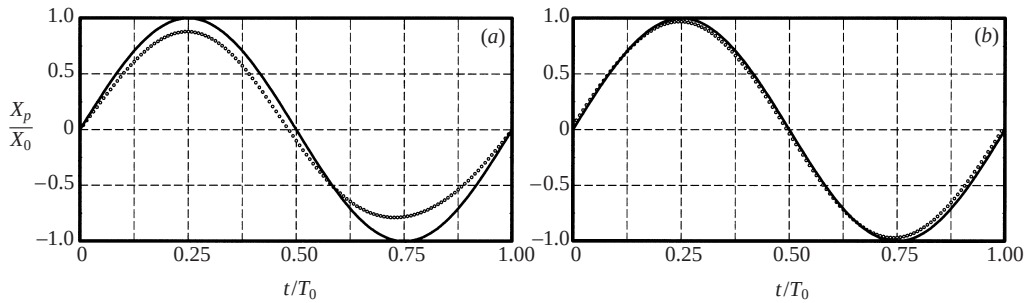

FIGURE 2. The continuous curve is the quasi-sinusoidal input signal to the stepper motor and the symbols denote the actual displacement of the piston measured using the LVDT. Dashed vertical lines show the phase positions used for phase-averaging the vorticity data. (*a*) $Re_0 = 10^3$, $St_0 = 0.072$; (*b*) $Re_0 = 10^4$, $St_0 = 0.0015$.

be the cross-sectional area of the tank, it can be deduced to first-order that

$$M = \int_{jet} u^2 \, \mathrm{d}A + U_R^2 A_R. \tag{3.2}$$

Finally, if the jet profile is approximately Gaussian and scales with η such that $u(x,\eta) = (BM^{1/2}/x)\exp[-C\eta^2/\eta_{1/2}^2]$, the return velocity is

$$U_R = \frac{2}{B} M^{1/2} x. \tag{3.3}$$

Substitution of this into the original balance gives a ratio between the jet momentum M and the source momentum of the form

$$\frac{M}{M_0} = \left[1 + \frac{16}{\pi B^2}\left(\frac{x}{D_0}\right)^2 \frac{A_0}{A_R}\right]^{-1}. \tag{3.4}$$

where A_0 is the cross-sectional area of the orifice. This analysis also neglects the effect of the riser tube at the end of the tank.

Positional feedback was obtained from a linear voltage displacement transducer (LVDT) which was directly mounted on the piston shaft. The driving velocity program to the stepper motor is closely approximated by a sinusoidal curve as shown by the displacement trace shown in figure 2.

The slight discrepancy between the driving signal and the actual motion of the piston is probably due to the presence of a flexible coupling between the stepper motor and the lead screw as shown in figure 1. This coupling consists of a strong helical spring which causes some lag in the motion of the piston and reduces the effective amplitude of the motion at low frequencies.

3.2. *Flow visualization*

The effect of the Reynolds number and Strouhal number on the structure of the ZNMF jet flow field was visualized using fluorescent dye. The flow visualizations were recorded using a Pulnix CCD camera and a VHS video recorder. The dye used for these experiments was Kiton Red 620, which fluoresces orange with a wavelength of 620 nm when illuminated by light with a wavelength of 532 nm. A plane containing the x,r-coordinates along the axis of the orifice of the flow was illuminated with a 200 mW continuous laser spread out into a sheet for these flow visualizations. Individual video frames were captured and digitized to a 256 level grey-scale image.

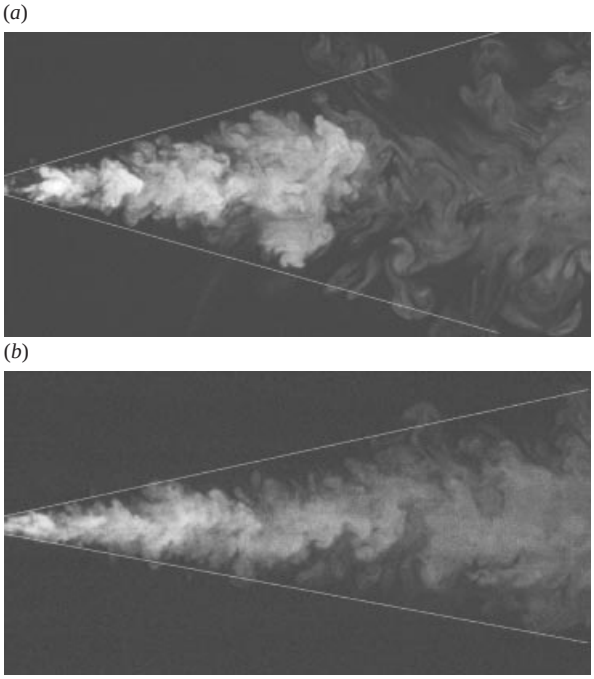

FIGURE 3. Digitized flow visualization of fluorescent dye marker for (*a*) a ZNMF jet, and (*b*) the equivalent continuous jet. The imaged domain measures $76D_0 \times 39D_0$. $Re_0 = 10^4$, $St_0 = 0.0015$. The light-coloured lines drawn on the images indicate the apparent mean boundary of the dye flow. The approximate spreading rates are: (*a*) $S_b \approx 0.13$, (*b*) $S_b \approx 0.1$.

An example of the resulting instantaneous images is shown in figure 3. These flow visualizations compare a ZNMF jet to an equivalent continuous jet based on momentum flow velocity. To preserve zero-net-mass injection during data acquisition, the dye was initially injected to displace the fluid in the cavity behind the orifice plate. The fluid was then left to settle for several minutes before the initiation of the piston motion. The relative spread of the jets is shown with lines that depict the mean boundary of the visible dye from a sequence of images. The apparent spreading rate for figure 3(*a*) for the ZNMF jet is $S_b \approx 0.13$ at $Re_0 = 10^4$, $St_0 = 0.0015$, compared to figure 3(*b*) in which $S_b \approx 0.1$ for the equivalent continuous jet.

3.3. *Multigrid cross-correlation PIV measurements*

For the PIV experiments the flow was seeded with nylon particles that have a nominal diameter of 28 μm. These tracer particles were illuminated by laser sheets produced from pulsed laser beams, which were generated by two Nd:YAG lasers that produce 400 mJ per pulse at a wavelength of 532 nm. These lasers have an intensity variation that is approximately Gaussian and a pulse duration of 6 ns. The pulse separation between the two lasers was set to 33 ms for these experiments. The two laser beams were set at orthogonal states of polarization and the beam paths were combined using a polarizing beam splitter plate. The combined beams were then passed through collimating optics which spread the 12 mm diameter beam into a sheet approximately 2 mm thick and 300 mm wide at the orifice. The laser sheets were much larger than the imaged region to minimize the effects of intensity variation across the images.

The PIV digital image acquisition was performed using a PCO SensiCam digital camera with a $1024 \times 1280\,\text{pixels}^2$ CCD array. Pairs of single-exposed images were analysed using multigrid cross-correlation digital particle image velocimetry (MCCD-PIV) analysis which is described in Soria (1996*a*, *b*, 1998) and Soria, Cater & Kostas (1999). This technique is not limited by either directional ambiguity or an inability to detect small displacements. The accuracy and uncertainty associated with multi-grid cross-correlation PIV and holographic PIV (HPIV) measurements have been investigated and are discussed in Soria (1998) and vonEllenrieder, Kostas & Soria (2001). The smallest cross-correlation window size used in the MCCDPIV analysis was $32 \times 32\,\text{pixels}^2$ and the separation between the MCCDPIV measurements was 16 pixels, resulting in vector grid of 61×61 vectors.

The individual realizations of the MCCDPIV measurements were used to calculate the mean velocity field. A nonlinear least-squares procedure was used to determine the Gaussian curve of best fit to the mean streamwise velocity profile $u_x(r)$ in order to estimate the peak velocity of the jet U_c, with better spatial resolution than the velocity field measurements. The value of the local jet half-width, $r_{1/2}$, was also determined from the Gaussian fit, which is expressed as

$$u_x(r) = U_c \exp\left[\frac{-C\eta^2}{\eta_{1/2}^2}\right]. \tag{3.5}$$

where $C = \ln(2)$ and $\eta_{1/2}$ is the half-width of the jet non-dimensionalized by the axial location.

3.4. *Vorticity calculation*

The out-of-plane vorticity was calculated from the MCCDPIV velocity field measurements using a local least-squares fit procedure to the velocity field, followed by analytic differentiation using the relationship $\omega_\theta = \partial u_x/\partial r - \partial u_r/\partial x$.

A thirteen-point, two-dimensional, local fit to the data was used (Soria 1996*b*). This calculation is an approximation that introduces additional bias and random error into the vorticity value. These errors have been investigated and discussed in Fouras & Soria (1998). The ratio of vorticity bias error to the exact value can be estimated from the relationship

$$\frac{\omega_{bias}}{\omega_{exact}} = -\frac{2}{3}\left(\frac{\Delta}{L}\right)^2 \tag{3.6}$$

which was derived in Cater (2002) using the technique outlined in Fouras & Soria (1998). This relationship shows that the bias error is related to the sampling separation between velocity measurements, where L can be thought as being a characteristic length scale of the vorticity distribution and Δ is the distance between adjacent velocity measurements.

The ratio of random error in the MCCDPIV velocity measurement compared to ω_θ is denoted by λ_0 and can be calculated using the following relationship derived in Cater (2002):

$$\lambda_0 = \sqrt{\frac{1}{7}}\left(\frac{L}{\Delta}\right). \tag{3.7}$$

This relation is specific to the thirteen-point fitting technique used to calculate the vorticity. For a vorticity distribution with a characteristic length scale of $4D_0$ the bias error is estimated as -6.2% and the random error is estimated as $\pm 6\%$ at the 95% confidence level.

3.5. *Jet momentum*

A measure of the relative appropriateness of an apparatus as a simulator for a free jet issuing into an unbounded domain is whether the velocity measurements satisfy the mean momentum integral equation. Hussein *et al.* (1994) give the inviscid second-order momentum integral equation as

$$M_I = 2\pi \int_0^\infty \left[u_x^2 + \overline{u_x'^2} - \tfrac{1}{2}\left(\overline{u_r'^2} + \overline{u_\theta'^2} \right) \right] r \, \mathrm{d}r. \tag{3.8}$$

From the planar PIV measurements it is possible to determine all of the terms on the right-hand side of equation (3.8) except $\overline{u_\theta'^2}$. However, previous investigations such as Hussein *et al.* (1994) and George & Hussein (1991) suggest that a good estimate for a round jet is $\overline{u_\theta'^2} \approx 0.5\overline{u_r'^2}$.

For the ZNMF jet, the value of the mean momentum flow through the orifice can be calculated using the momentum flow velocity defined in equation (2.3). This gives the result

$$M_0 = \frac{\pi}{4} D_0^2 U_0^2. \tag{3.9}$$

3.6. *Entrainment*

A quantity of particular importance in the application of jet flows is the rate of entrainment of ambient fluid by the jet. For the case of a continuous jet, the mass of entrained fluid per unit length (i.e. $\rho\varepsilon$) can be calculated by integrating the continuity equation

$$\varepsilon = \lim_{r\to\infty}(-2\pi r u_r) = \frac{\mathrm{d}}{\mathrm{d}x}\left[2\pi \int_0^\infty u_x r \, \mathrm{d}r \right]. \tag{3.10}$$

Previous experimental studies have indicated a mean value for the integral of $\varepsilon/D_0 = 0.14U_c$ (Piquet 1999).

To investigate changes in the rate of entrainment, profiles of mean radial velocity were extracted from the PIV velocity field measurements which were then plotted as a function of streamwise distance. The mean radial velocity is pre-multiplied by the radial coordinate to account for the increase in surface area of a cylinder enclosing the jet and non-dimensionalized with the momentum flow velocity and the orifice diameter.

An alternative measure of the entrainment is the coefficient proposed by Morton, Taylor & Turner (1956). Hussein *et al.* (1994) provide the following expression for the entrainment coefficient α_ε, for a self preserving jet:

$$\alpha_\varepsilon = \frac{I_1}{2(I_2)^{1/2}}, \tag{3.11}$$

where I_1 and I_2 are defined by

$$I_1 = 2\int_0^\infty \left(\frac{u_x}{U_c} \right) \eta \, \mathrm{d}\eta, \tag{3.12}$$

$$I_2 = 2\int_0^\infty \left(\frac{u_x}{U_c} \right)^2 \eta \, \mathrm{d}\eta. \tag{3.13}$$

	Re_0	St_0	L_D	Δ/D_0	$\Delta t_1/T_0$	$\Delta t_2/T_0$	n	N
Continuous jet	10^4	–	–	0.95	0.0008	0.88	64	1024
ZNMF jet	10^4	0.0015	150	0.95	0.0016	0.88	64	1024

TABLE 1. Far-field jet investigation parameters.

	Re_0	St_0	L_D	Δ/D_0	$\Delta t_1/T_0$	$\Delta t_2/T_0$	n	N
ZNMF jet	10^4	0.0015	150	0.45	0.0016	0.20	64	1024
ZNMF jet	10^3	0.0072	62.5	0.46	0.1316	0.88	64	1024

TABLE 2. Near-field jet investigation parameters.

4. Experimental parameters

For the purposes of this investigation the flow domain has been divided into two regions: the far field which extends from an axial distance of $30D_0$ to the limits of the apparatus, and the near field which extends from the generator to a distance of $30D_0$.

A turbulent ZNMF jet with the smallest Reynolds number found in the flow visualization study was selected for further study, due to the limitations of the experimental technique. This was compared to a continuous jet at $Re_0 = 10^4$ and existing published findings. A transitional jet at $Re_0 = 10^3$ was also selected for the near-field study to verify the results presented in Cater, Bertillino & Soria (1999) and Cater & Soria (2000). The range of Strouhal numbers for these jets was limited by the stepper motor.

The mean velocity profiles of the ZNMF jets show a self-similar collapse at approximately $x/D_0 = 15$. However, the far field of the jets was defined from the axial location at which the Reynolds stresses show self-similar behaviour, which is further downstream at approximately $x/D_0 = 25$.

4.1. *Far-field measurements*

The first set of experiments investigated the self-similar behaviour of the flow in the developed region of the jets. The imaged area was rectangular and measured $80D_0$ downstream from the orifice and $32D_0$ in the radial direction for the investigation of the far field. Table 1 shows the experimental parameters used in the jet far-field study, where n is the number of images acquired in a sequence and N is the total number of image pairs recorded. The time between image frames is Δt_1, between image pairs Δt_2 and the period of the oscillations is $T_0 = 250$ ms. The measurement area of each MCCDPIV velocity vector $1.9D_0 \times 1.9D_0$ and the separation between the velocity vectors is $\Delta = 0.95D_0$ in this region. To ensure that a statistically stationary flow is achieved, there is a delay of 60 s between the initiation of motion and the beginning of the measurement recording. This time is limited by the maximum stroke of the piston during continuous jet generation which is 94 s at $Re_0 = 10^4$.

4.2. *Near-field measurements*

To investigate the evolution of turbulent quantities in the flow development region, a smaller region of interest was selected that was located at the orifice exit and measured $40D_0$ downstream of the orifice and $16D_0$ in the radial direction for the near-field study. Table 2 shows the parameters used for the investigation of the near-field velocity measurements. The measurement area of each MCCDPIV velocity

vector is $0.9D_0 \times 0.9D_0$ and the velocity sample separation is $\Delta/D_0 = 0.45$ in this region.

4.3. *Phase-average measurements*

A signal from the positional encoder was used to trigger the acquisition of pairs of single-exposed digital images at different points in the oscillation cycle of the ZNMF jet to obtain phase-locked data. The phase positions were measured from the rearmost actuator position. These phases are $t/T_0 = 0$, 1.25, 0.250, 0.375, 0.500, 0.625, 0.750 and 0.875. The resultant velocity measurements were averaged at each phase to produce phase-averaged MCCDPIV measurements. The phase-averaged velocity fields were then used to calculate out-of-plane vorticity fields $\omega_\theta(x,r)$, which when examined revealed the formation sequence of the ZNMF jet in the near field with $Re_0 = 10^3$. Examples of phase-triggering used for the acquisition of PIV data can be found in Panchapakesan & Soria (1999) and Cater, von Ellenrleder & Soria (2001).

The acquisition parameters for the jets are the same as those shown in table 2, except that $\Delta t_2 = T_0$. To ensure that the flow is developed in the tank, there was a delay of 30 min before the start of image recording.

5. Results

5.1. *Flow visualization*

The initial flow visualizations shown in figure 3 revealed that the spreading rate of a round turbulent ZNMF jet is greater than an equivalent continuous jet throughout the measured domain. From a small jet at the orifice, a turbulent ZNMF jet flow spreads rapidly, and in the far field, structures with length scales many times that of the orifice are present. Also visible are ring-like structures at the boundary of both jets. There is some evidence of greater entrainment for the ZNMF jet in this figure, which can be seen as the penetration of (darker) ambient fluid. However, care must be taken in interpreting dye remnants since the dye used in the experiments diffuses away from regions of high vorticity and thus there may be no vorticity associated with regions of relatively high dye concentration. For a highly intermittent flow, it is likely that the spread of the jet will be over-estimated using dye, since dye will persist in regions where vorticity has dissipated.

A number of different flow patterns were observed in the dye visualization study:

(*a*) At low Reynolds numbers and relatively high Strouhal numbers, the flow is an apparently steady stream of dye flowing from the orifice with little penetration of ambient fluid as shown in figure 4(*a*); this is termed a laminar jet. This regime has not been reported previously in any of the available experimental or numerical literature.

(*b*) The term 'laminar rings' has been used where the flow field consists of individual identifiable laminar vortex rings generated at the forcing frequency as shown in figure 4(*b*). In this flow successive rings produced at the orifice are influenced by the path of preceding rings, but they do not coalescence within the observable flow domain.

(*c*) As the Reynolds number is increased the rings begin to coalesce within the observable domain and an erratic, intermittent jet forms as shown in figure 4(*c*); this type of transitional flow is termed a 'transitional jet'.

(*d*) At the highest Reynolds numbers there is a large range of scales observed in the flow as shown in figure 4(*d*). This is termed a 'turbulent jet' and it is very similar in appearance to a conventional continuous turbulent jet.

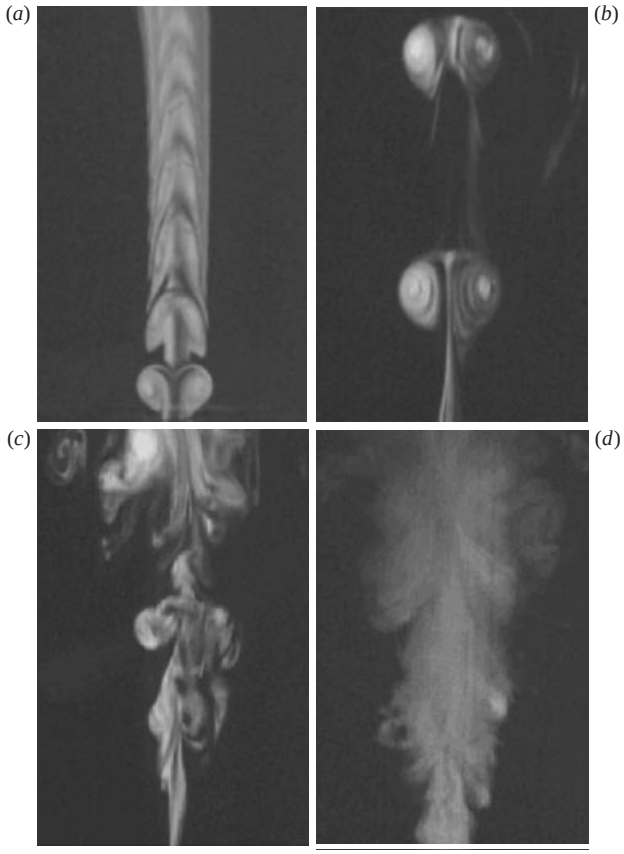

FIGURE 4. Digitized video realizations of ZNMF jet flow patterns: (*a*) laminar jet $Re_0 = 3336$, $St_0 = 0.03$, $S_b \approx 0.05$; (*b*) a series of laminar rings, $Re_0 = 7784$, $St_0 = 0.012$, $S_b \approx 0.06$; (*c*) a transitional jet, $Re_0 = 11\,121$, $St_0 = 0.009$, $S_b \approx 0.1$; and (*d*) a turbulent jet, $Re_0 = 66\,991$, $St_0 = 0.009$, $S_b \approx 0.13$.

The complete results of the flow visualization study are summarized in the parameter map shown in figure 5. As the source Reynolds number is increased for a constant Strouhal number an initially laminar jet breaks into individual rings that become turbulent and eventually coalesce to produce a turbulent jet flow. For a constant source Reynolds number, increasing the Strouhal number effectively decreases the spacing between successive rings. At high Strouhal numbers (i.e. $St_0 > 3 \times 10^{-2}$) a jet-like pattern always forms, although the nature of the jet is dependent upon the Reynolds number. At low Strouhal number (large amplitude), further complexities in the flow structure may arise from secondary rings that form from disturbances in the shear layer behind the leading vortex ring. In comparison, the typical range of parameters for micro-fluidic devices or micro-electro-mechanical-systems (MEMS) is $Re_0 \approx 10^2$ and $St_0 \approx 10^0$ (Coe *et al.* 1994).

5.2. *Far-field measurements*

For a self-similar turbulent continuous jet, the angle of spread and the rate of jet decay can be determined from dimensional analysis to be approximately independent of the source Reynolds number in the far field. Piquet (1999) indicates a typical value for B of between 6 and 7 for most facilities at high Reynolds numbers ($> 10^4$).

	Re_0	S_u	B	$\eta_{1/2}$
Analytical model	–	0.167	6.66	0.100
Wygnanski & Fiedler (1969)	10^5	0.176	6.40	0.086
Hussein *et al.* (1994)	10^5	0.172	6.56	0.094
Panchapkesan & Lumley (1993)	10^4	0.165	6.84	0.096
Present result: continuous jet	10^4	0.178	6.32	0.092
Present result: ZNMF jet	10^4	1.213	0.93	0.107

TABLE 3. Jet far-field properties, $x = 60D_0$.

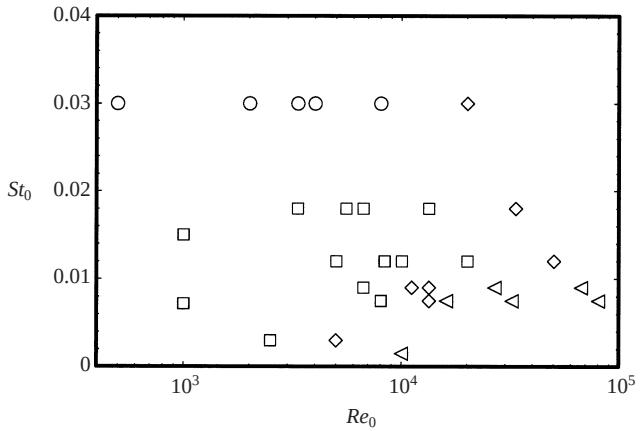

FIGURE 5. Summary of ZNMF jet flow patterns classified from video sequences of dye flow and plotted as a function of Strouhal number and source Reynolds number. Different symbols represent different flow patterns: laminar jets (○), laminar rings (□), transitional jets (◇) and turbulent jets (◁).

The theoretical value for a top-hat initial velocity distribution in an unbounded flow is 6.66. A similar Reynolds number independence was expected for the far field of turbulent ZNMF jets.

The mean properties of the turbulent ZNMF jet and a comparable continuous jet are shown in table 3 compared to the analytical values for the top-hat profile. The LDA measurements of Hussein *et al.* (1994) are also shown since these data satisfy the equations of motion to second order, and can be regarded as being representative of real unconfined axisymmetric jets. The data of Panchapkesan & Lumley (1993) are at a similar Reynolds number to the data in this paper.

The behaviour of the continuous jet at $Re_0 = 10^4$ is roughly consistent with the data of Hussein *et al.* (1994) which adds credibility to the measurement technique. An increase in the spread for the continuous jet above the data of Wygnanski & Fiedler (1969) may be accounted for by the Reynolds number difference, as explained in Panchapkesan & Lumley (1993). However, the decay of the ZNMF jet is seven times greater than the continuous jet in this facility. These measurements also confirm the inference from the flow visualization that the spreading rate of the ZNMF jets is greater.

Figure 6 shows profiles of mean axial velocity for the ZNMF jet and the equivalent continuous jet at an axial distance of $60D_0$. The velocity is non-dimensionalized by U_0 and the radial displacement is non-dimensionalized by D_0. This figure shows the

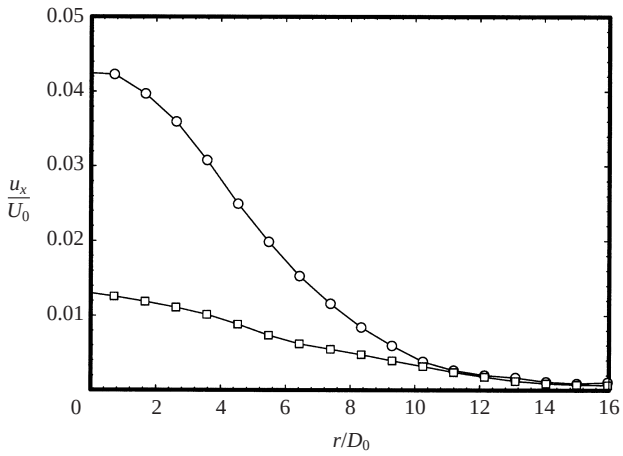

FIGURE 6. Non-dimensionalized (but non-normalized) profiles of axial velocity $\overline{u_x}/U_0$, at $x = 60D_0$ for jets at $Re_0 = 10^4$. Continuous jet (○), ZNMF jet, $St_0 = 0.0015$ (□).

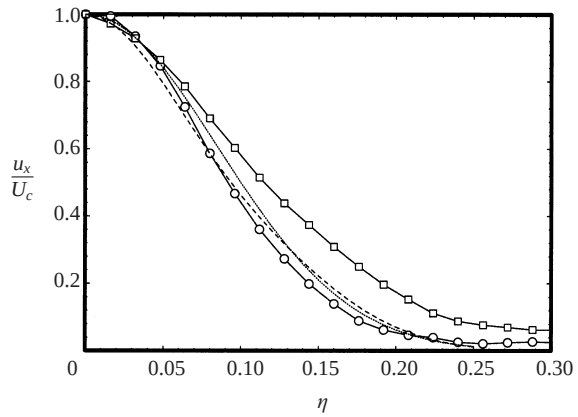

FIGURE 7. Normalized profiles of axial velocity $\overline{u_x}/U_c$, at $x = 60D_0$ for jets at $Re_0 = 10^4$. Continuous jet (○), ZNMF jet, $St_0 = 0.0015$ (□), Gaussian distribution (···), Hussein *et al.* (1994) (– –).

difference in the mean far-field flow. The centreline velocity for the continuous jet at $x = 60D_0$ is $U_c = 0.225\,\mathrm{m\,s^{-1}}$. For the ZNMF jet the centreline velocity is $U_c = 0.069\,\mathrm{m\,s^{-1}}$. Thus the continuous jet has a centreline velocity that is approximately 4 times greater than the ZNMF jet at $x = 60D_0$. The half-width of the continuous jet is approximately $r_{1/2} = 5D_0$, whereas the ZNMF jet has a half-width closer to $r_{1/2} = 6D_0$.

Figure 7 shows the same data as figure 6, normalized by the centreline velocity and the similarity variable. This is the conventional scaling for the radial direction, as used by Wygnanski & Fiedler (1969) and Hussein *et al.* (1994). The velocity fit to the data of Hussein *et al.* (1994) and the Gaussian profile given by equation (3.5) are also shown for comparison. The continuous jet distribution has a Gaussian shape, though the profile is narrower than the experimental curve fit of Hussein *et al.* (1994). This result is consistent with a loss in jet momentum. The difference between these distributions is most noticeable between $0.1 \leqslant \eta \leqslant 0.2$. The ZNMF has a greater non-dimensional half-width, as shown in table 3, and a consistently higher value of

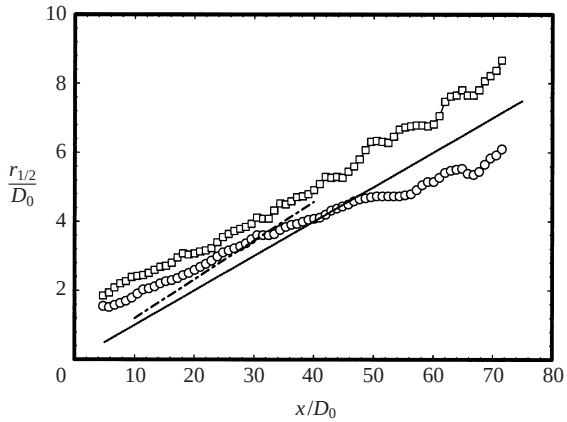

FIGURE 8. Non-dimensionalized evolution of the jet half-width at $Re_0 = 10^4$. Continuous jet (○), ZNMF jet, $St_0 = 0.0015$ (□). A line with the theoretical gradient for a top-hat initial velocity profile is shown (· · ·) as well as the empirical fit from Bremhorst & Hollis (1990) for fully pulsed jets (– · –).

$\overline{u_x}/U_c$. The value of $\overline{u_x}/U_c$ is positive throughout the measurement domain and thus it is concluded that the imaged domain was too small to measure the reverse flow that surrounds the jets.

Figure 8 shows the evolution of the jet half-width as a function of axial distance for the two jets compared to the theoretical spread of an unbounded jet. The evolution of $r_{1/2}$ for both jets increases linearly up to $x = 30D_0$. However, both curves depart from the expected relationship beyond this location in a different manner. The rate of increase in half-width of the continuous jet decreases steadily throughout the far field. Conversely, beyond $x = 30D_0$, the spread of the ZNMF jet increases slightly. This behaviour is attributed to the geometry of the apparatus, specifically the lateral confinement. The endwall has progressively more influence on the flow with increasing axial distance.

An empirical fit to the data of Bremhorst & Hollis (1990) is also displayed, $r_{1/2} = 0.1125x - 0.071$. This fit is only valid in the range $10 \geqslant x/D_0 \geqslant 40$, but demonstrates that pulsed jets have an even greater spreading rate than either the ZNMF jet or the continuous jet. The irregular nature of the curves at large axial distances despite the relatively large number of samples ($> 10^3$), reflects the intermittent nature of structures at the boundary of both jets.

Figure 9 shows the mean vorticity contours for the continuous jet at $Re_0 = 10^4$ and an equivalent ZNMF jet at $St_0 = 0.0015$. The general shape of both distributions is the same, despite the different mechanisms responsible for the jet formation. The mean vorticity contours of the continuous jet have a magnitude which is approximately twice that of the ZNMF jet. The vorticity values in the near-field region are considerably lower than expected when $x < 10D_0$. These low values can be explained by the MCCDPIV analysis methodology.

The MCCDPIV measurements in the region around the orifice were unreliable, due to the high velocity gradients that are present there and the operational limitations of the digital CCD camera used in these experiments. Therefore, the measurements in this region are prone to large errors as indicated in Soria (1998). For this reason the measurements in this region were rejected, which has resulted in the presentation of incomplete velocity field and thus erroneous vorticity values.

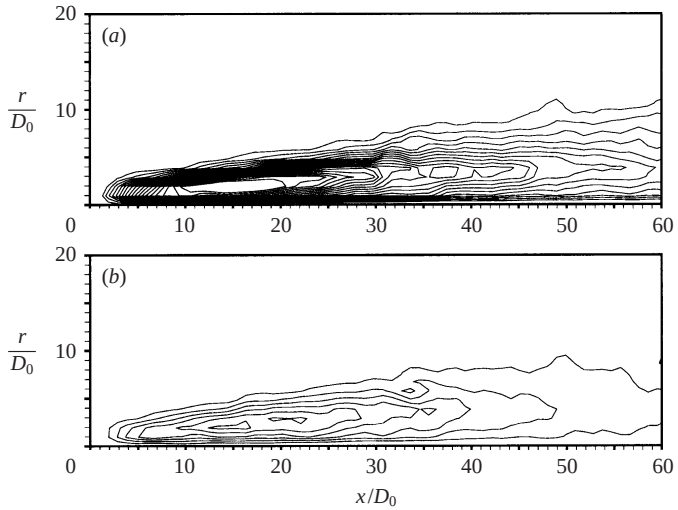

FIGURE 9. Mean, non-dimensional vorticity $\overline{\omega_\theta} D_0/2U_0$ at contour levels of 5×10^{-4}, for jets at $Re_0 = 10^4$. (*a*) Continuous jet, (*b*) ZNMF jet, $St_0 = 0.0015$.

5.3. *Near-field measurements*

To explain the measured differences in the far-field behaviour for ZNMF jets, a study was conducted of the near field of the ZNMF jets using PIV. One thousand and twenty four image pairs were captured and analysed to determine the spatial dependence of the flow quantities. Profiles of the components of velocity versus axial distance are shown in figure 10. These quantities are scaled with the local maximum velocity and the similarity variable.

In figure 10(*a*), the mean axial component of velocity u_x shows an almost immediate collapse to Gaussian-like profile, which is typical of a round continuous jet as described in Rajaratnam (1976). In contrast, the mean radial component u_r shown in figure 10(*b*), exhibits an interesting trend. Although the general shape of the profiles is consistent with other jet data, the magnitude is initially small. The magnitude of the radial velocity then increases to a maximum near $x = 15D_0$, before a reduction takes place, and finally a self-similar collapse develops at $25D_0$. The radial velocity profiles have a degree of asymmetry, which suggests a slight mean radial velocity component for the entire jet.

The most probable cause of this asymmetry in the near-field flow is geometric asymmetries in the bevelled edge of the orifice plates produced during manufacture. The riser tube may also be the cause of asymmetries in the mean flow further downstream, in particular the mean radial velocity. With the riser tube open to the atmosphere, the necessity of a mean reverse flow around the continuous jet is removed and so the far field of the continuous jet measurements is most likely to be affected by the free surface.

Figure 10(*c*) shows the streamwise profiles of the mean out-of-plane vorticity, which has been non-dimensionalized using the local centreline velocity and the jet half-width. Profiles of the mean vorticity also collapse and exhibit a self-similar scaling at streamwise locations beyond $15D_0$. The spatial distribution of vorticity is examined in more detail in § 5.6.

Profiles of the in-plane Reynolds stresses are shown in figure 11. The maximum magnitude of the fluctuating component of axial velocity $\overline{u_x'^2}$ shown in fig-

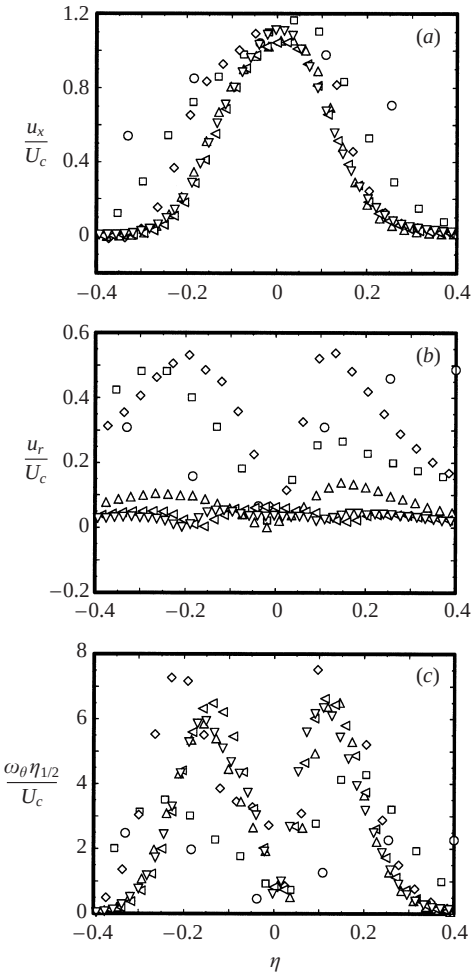

FIGURE 10. Non-dimensionalized streamwise profiles of mean velocity components and vorticity in the developing region of a ZNMF jet, $Re_0 = 10^3$, $St_0 = 0.0072$. U_c is the peak jet velocity determined from a Gaussian fit and axial location. Different symbols represent different axial locations: $x/D_0 = 5$ (○), 10 (□), 15 (◇), 20 (△), 25 (◁), 30 (▽).

ure 11(*a*) has the same trend as the maximum magnitude of the radial velocity, with a local maximum at $x = 15D_0$. The shape of the profiles of the fluctuating component of the radial velocity $\overline{u_r'^2}$ shown in figure 11(*b*) is almost identical to the axial component, but has approximately half their magnitude. The turbulent shear stress $\overline{u_x' u_r'}$ shown in figure 11(*c*) has a similar profile to the vorticity distribution in figure 10(*c*), but there is considerably more scatter in the data, which reflects the need for a greater number of samples to reduce the uncertainty in the higher-order statistics. The self-similar collapse and distribution of all the profiles shown in figures 10 and 11 for the round jet is similar to the corresponding measurements for the planar ZNMF jets (Smith & Glezer 1998).

Profiles of the components of velocity versus radial distance are shown in figure 12 for the two ZNMF jets at $x = 30D_0$. These quantities are scaled with the source velocity and the orifice diameter. The centreline velocities are $U_c = 11.6 \times 10^{-3}\,\mathrm{m\,s^{-1}}$ ($Re_0 = 10^3$) and $U_c = 122 \times 10^{-3}\,\mathrm{m\,s^{-1}}$ ($Re_0 = 10^4$). From these values it appears that

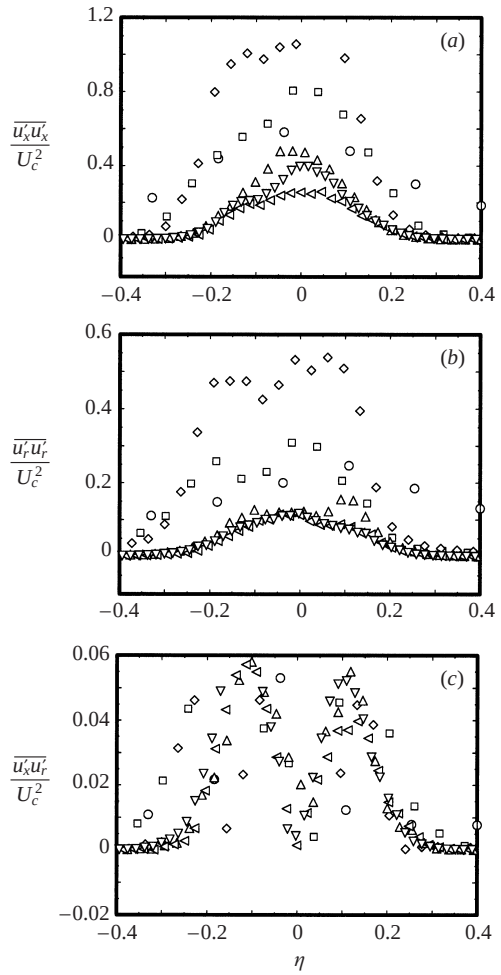

FIGURE 11. Non-dimensionalized Reynolds stresses in the developing region of a ZNMF jet, $Re_0 = 10^3$, $St_0 = 0.0072$. The Reynolds stresses are scaled with the square of the local jet centreline velocity. Radial position is non-dimensionalized by the axial location. Different symbols represent different axial locations: $x/D_0 = 5$ (○), 10 (□), 15 (◇), 20 (△), 25 (◁), 30 (▽).

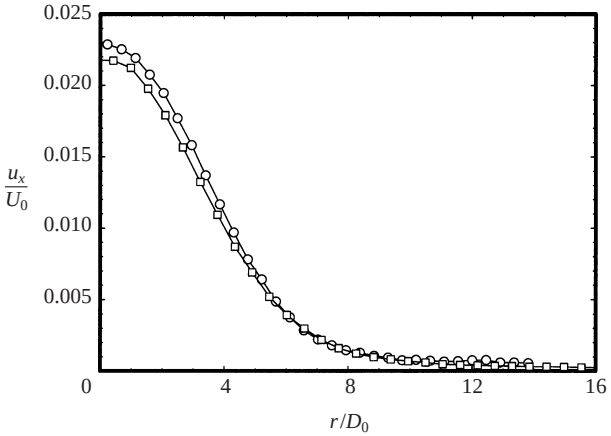

FIGURE 12. Non-dimensional profiles of axial velocity $\overline{u_x}/U_0$, at $x = 30D_0$. $Re_0 = 10^3$, $St_0 = 0.0072$ (□), $Re_0 = 10^4$, $St_0 = 0.0015$ (○).

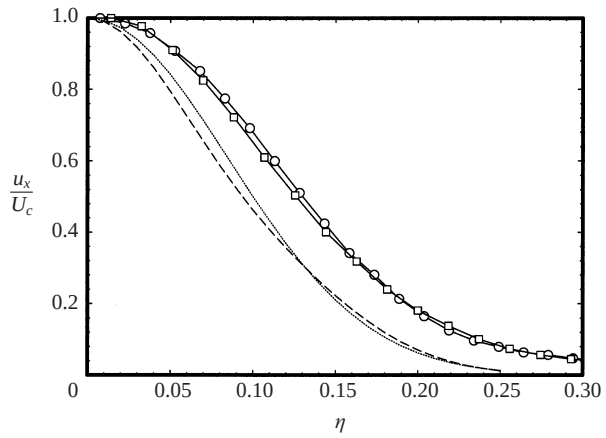

FIGURE 13. Normalized profiles of axial velocity $\overline{u_x}/U_c$, at $x = 30D_0$. $Re_0 = 10^3$, $St_0 = 0.0072$ (□), $Re_0 = 10^4$, $St_0 = 0.0015$ (○), Gaussian distribution (· · ·), Hussein *et al.* (1994) (– –).

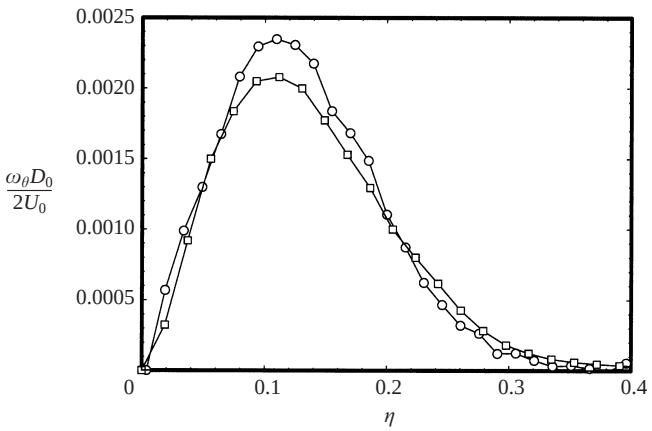

FIGURE 14. Non-dimensionalized streamwise profiles of vorticity $\overline{\omega_\theta}$, at $x = 30D_0$. $Re_0 = 10^3$, $St_0 = 0.0072$ (□), $Re_0 = 10^4$, $St_0 = 0.0015$ (○).

the mean centreline velocity scales linearly with the Reynolds number as expected. The Reynolds number difference appears to have little discernible effect on the mean velocity profile since the shape of both profiles is similar and the half-width of both jets is approximately $r_{1/2} = 3.9D_0$ at $x = 30D_0$. Once again, it appears that the measurement domain is too small to capture the mean reverse flow.

Figure 13 shows the normalized velocity profiles for the data shown in figure 12 at $x = 30D_0$. The ZNMF jet with $Re_0 = 10^4$ has a slightly higher non-dimensional centreline velocity, but the half-width of the two jets is nearly identical. The profiles of both jets exhibit a self-similar collapse. The shape of the profiles confirms that the spreading rate of the ZNMF jets in this enclosure is approximately 20% greater than the analytical model and the experimental measurements of Hussein *et al.* (1994) for an unbounded continuous jet.

Figure 14 shows streamwise profiles of the mean out-of-plane vorticity, which has been scaled by the source velocity and the orifice diameter. Profiles of the mean vorticity also collapse and exhibit a self-similar scaling at streamwise locations beyond $15D_0$. At $x = 30D_0$ the shape of the profiles is similar, but the jet with $Re_0 = 10^4$ has

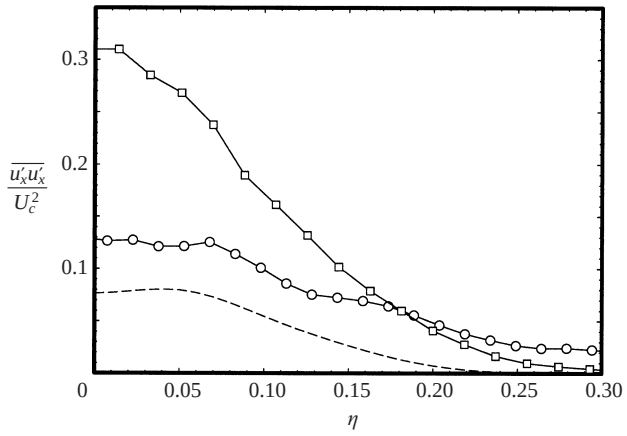

FIGURE 15. Fluctuating axial velocity profile $\overline{u_x'^2}/U_c^2$, at $x = 30D_0$. $Re_0 = 10^3$, $St_0 = 0.0072$ (□), $Re_0 = 10^4$, $St_0 = 0.0015$ (○), Hussein *et al.* (1994) (– –).

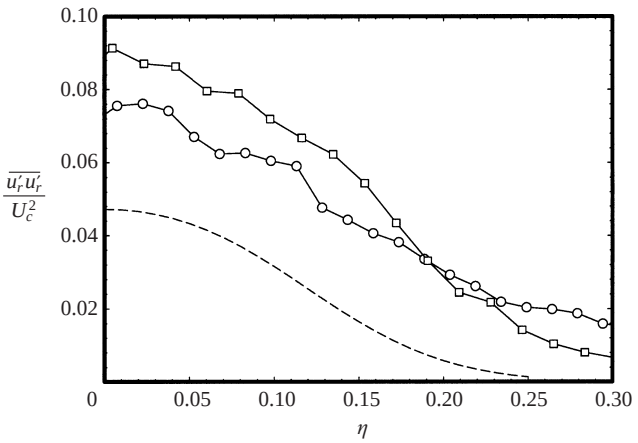

FIGURE 16. Fluctuating radial velocity profile $\overline{u_r'^2}/U_c^2$, at $x = 30D_0$. $Re_0 = 10^3$, $St_0 = 0.0072$ (□), $Re_0 = 10^4$, $St_0 = 0.0015$ (○), Hussein *et al.* (1994) (– –).

a peak value which is 10% higher. However, the estimated error in the peak value is considerably higher for the lower Reynolds number jet. The spatial distribution of vorticity is examined in more detail in § 5.6.

Profiles of the in-plane Reynolds stresses, $\overline{u_x'^2}$, $\overline{u_r'^2}$ and $\overline{u_x'u_r'}$ are shown in figures 15, 16 and 17 respectively. The Reynolds stresses are non-dimensionalized by the square of the centreline velocity, $U_c^2 = 5.24 \times 10^{-4} U_0^2$ ($Re_0 = 10^4$) and $U_c^2 = 4.75 \times 10^{-4} U_0^2$ ($Re_0 = 10^3$). The non-dimensional centreline values for the normal stresses $\overline{u_x'}^2$ and $\overline{u_r'}^2$ are: 0.13 and 0.07 ($Re_0 = 10^4$), and 0.31 and 0.09 ($Re_0 = 10^3$) respectively.

The value of the root-mean-square fluctuating axial velocity at the centreline is $u'_{xRMS} = 0.36$ for the ZNMF jet at $Re_0 = 10^4$, which is very similar to the value of $u'_{xRMS} = 0.35$ obtained by James *et al.* (1996) and 50% greater than the value of $u'_{xRMS} = 0.28$ found by Wygnanski & Fiedler (1969) and Hussein *et al.* (1994) in the far field of a continuous jet. The centreline fluctuating axial velocity when $Re_0 = 10^3$ is higher again, with a value of $u'_{xRMS} \approx 0.56$. This may be an indication of the presence of large-scale structures that are convected along the axis of the jet. This suggests

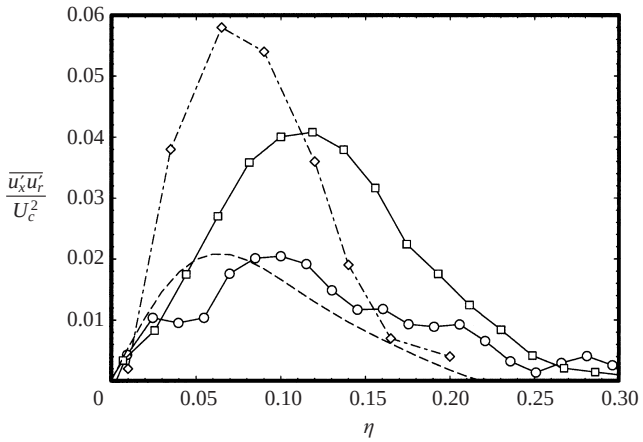

FIGURE 17. Non-dimensionalized turbulent Reynolds stresses $\overline{u_x'u_r'}/U_c^2$, at $x = 30D_0$. $Re_0 = 10^3$, $St_0 = 0.0072$ (□), $Re_0 = 10^4$, $St_0 = 0.0015$ (○), Hussein *et al.* (1994) (– –). The experimental data of Bremhorst & Hollis (1990) at $x = 30D_0$ for fully-pulsed jets are also shown (◇). (Reproduced with permission of the authors.)

that the effect of the oscillations persists further downstream as coherent structures at lower Reynolds numbers. The fluctuating axial velocity profile shown in figure 15 also exhibits the slight off-axis bulge seen in the continuous jet data of Hussein *et al.* (1994) and Panchapkesan & Lumley (1993).

The shape of profiles of the fluctuating component of radial velocity $\overline{u_r'^2}$, shown in figure 16 is almost identical to the axial component, but has approximately half the magnitude. This ratio is consistent with previous measurements. The radial symmetry of the flow requires that the unknown component $\overline{u_\theta'^2}$ is equal to half the radial stress, $\overline{u_r'^2}$. This condition is verified for the unbounded jet in Hussein *et al.* (1994). The values of $\overline{u_r'^2}$ shown in figure 16 are much higher than expected across the jets. This is attributed to the passage of relatively large-scale rotational motions which are seen in the flow visualization.

The far-field turbulent shear stress $\overline{u_x'u_r'}$ shown in figure 17 has a similar profile to the near-field distribution in figure 10(*c*). The Reynolds stress measurements of Bremhorst & Hollis (1990) for fully pulsed jets at $Re_0 = 6 \times 10^4$ are also shown in figure 17 for comparison. The values of the turbulent shear stress for the ZNMF jets are higher than the continuous jet and lower than that measured by Bremhorst & Hollis (1990) for fully pulsed jets.

The scatter is evidence that a greater number of samples is required to reduce the uncertainty of the second-order statistics. It appears that the number of samples acquired is large enough to reach an acceptable uncertainty in the time averages of velocities, but too small to reach a low uncertainty in the second moments of velocity fluctuations (Tennekes & Lumley 1972), particularly at $Re_0 = 10^4$. The peak value of $\overline{u_x'u_r'} = 0.02$ at $Re_0 = 10^4$ is found to be consistent with the data of Panchapkesan & Lumley (1993).

5.4. *Momentum integrals*

The measured values for the components of the second-order momentum integral are shown in table 4 compared to the analytical values for the top-hat profile. The different value of $\overline{u_x'}^2$ for $Re_0 = 10^4$ is partly due to the experimental technique. As

	Re_0	$\overline{u_x}^2$	$\overline{u_x'^2}$	$\overline{u_r'^2}$	$\overline{u_\theta'^2}$	M_I/M_j
Hussein *et al.* (1994)	10^5	0.87	0.24	0.13	0.15	0.97
Present result: ZNMF jet	10^4	0.63	0.26	0.14	–	0.79
Present result: ZNMF jet	10^3	0.83	0.42	0.23	–	1.08

TABLE 4. Jet momentum integrals.

	Re_0	I_1	I_2	α_ε
Gaussian model	–	0.014	0.0072	0.084
Ricou & Spalding (1961)	10^5	–	–	0.080
Hussein *et al.* (1994)	10^5	0.014	0.0066	0.081
Present result: continuous jet	10^4	0.014	0.0063	0.089
Present result: ZNMF jet	10^4	0.021	0.0092	0.107

TABLE 5. Jet entrainment coefficient.

explained previously, the ZNMF jet is broader at each section, and the region that could be imaged with the digital camera does not capture the entire jet flow. The larger return flow observed for a ZNMF jet also reduces the possible momentum of the jet. This momentum deficit at $Re_0 = 10^4$ can also be explained by the components ignored in equation (3.8), in particular the viscous terms. An alternative, suggested by Smith & Glezer (1998), was that the discrepancy is due an adverse streamwise pressure gradient in the vicinity of the orifice. A conventional analysis of the jet flow assumes that the pressure gradient is negligible; however, there always exists a net difference in hydrostatic pressure to establish the flow. Unfortunately, PIV does not permit the measurement of the pressure field. This is the most compelling reason to study the evolution of the vorticity field.

The main difference in the relative magnitude of the three components at $Re_0 = 10^3$ is the unusually high proportion of the jet momentum in the axial component of turbulent kinetic energy $\overline{u'^2}$. This is not entirely unexpected, since this is the mode of forcing the flow. Energy is transferred from this component to all others. The radial component of the ZNMF jet is in close agreement with previously published data for the continuous jet (Hussein *et al.* 1994). An estimate of the error associated with these quantities is presented in § 5.7.

5.5. *Entrainment*

It is well-established that the entrainment rate of a round turbulent continuous jet increases approximately linearly in the developing region up to the end of the potential core at approximately $12D_0$ (Ricou & Spalding 1961). Beyond this point a steady value is reached. The measurements of Hussein *et al.* (1994) indicate a steady value of $\varepsilon/D_0 = 0.14U_c$.

Table 5 shows the values of the streamwise profile integrals and the entrainment coefficient of Morton *et al.* (1956). The entrainment coefficient for the continuous jet is 10% greater than expected. Again, this increase in entrained fluid is consistent with a loss of momentum, due to the bounded nature of the flow within this facility. For the ZNMF jet the entrainment coefficient is 20% larger than the value of $\alpha_\varepsilon = 0.08$ obtained by direct measurement with a porous cylinder in Ricou & Spalding (1961).

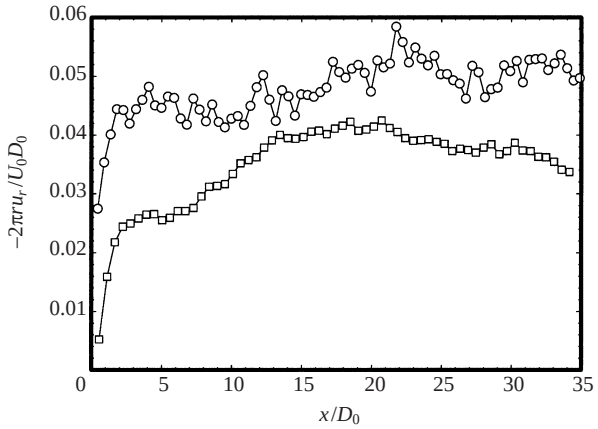

FIGURE 18. Mean, non-dimensionalized radial velocity for ZNMF jets $-2\pi r\overline{u_r}/U_0 D_0$, at $r = 10D_0$. $Re_0 = 10^3$, $St_0 = 0.0072$ (□), $Re_0 = 10^4$, $St_0 = 0.0015$ (○).

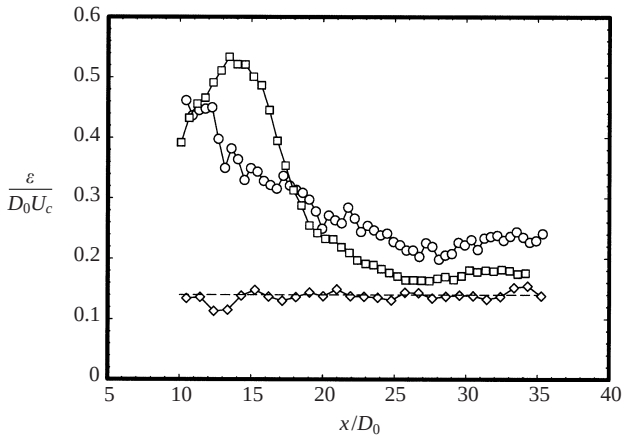

FIGURE 19. Mean, normalized entrainment velocity for ZNMF jets $\varepsilon/D_0 U_c$. $Re_0 = 10^3$, $St_0 = 0.0072$ (□), $Re_0 = 10^4$, $St_0 = 0.0015$ (○), continuous jet $Re_0 = 10^4$ (◇) and $\varepsilon/D_0 = 0.14U_c$ (– –).

The value of 0.08 was also obtained by Hussein *et al.* (1994) using LDA and a flying hot wire.

The mean radial velocity for the ZNMF jet at $Re_0 = 10^3$ and $St = 0.0072$ is shown in figure 18 as a function of axial distance. At axial distances larger than $15D_0$, the radial velocity decays with increasing distance. However, close to the orifice plane a different trend is observed due to the influence of the boundary layer flow at the orifice plane. The radial velocity at each section also provides the most reliable estimate of the axial volume flow using the principle of the conservation of mass.

Figure 19 shows the entrainment velocity in the near field of the ZNMF jets and the continuous jet at $Re_0 = 10^4$, normalized by the centreline velocity. Reliable centreline velocity data are unavailable in the region where $x < 10D_0$, due to the volume-averaged nature of the measurements. The asymptotic values for the ZNMF jets are $\varepsilon/D_0 = 0.18U_c$ ($Re_0 = 10^4$) and $\varepsilon/D_0 = 0.24U_c$ ($Re_0 = 10^3$). The continuous jet maintains the expected value of $\varepsilon/D_0 = 0.14U_c$.

Figure 20 shows the evolution of the mean centreline velocity in the near-field region: it is expected to progress from a value of zero at the orifice exit, to a

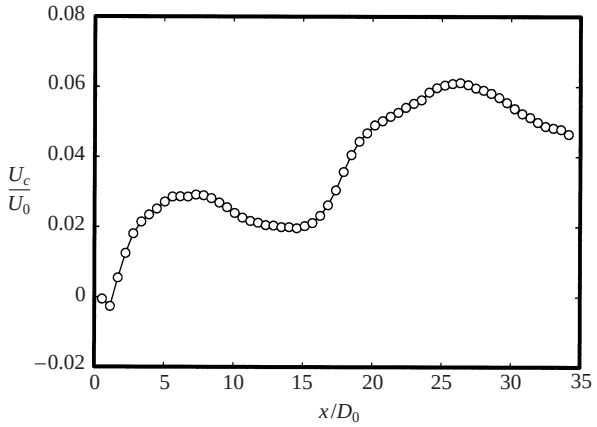

FIGURE 20. Non-dimensionalized mean centreline velocity as a function of stream-wise distance in the developing region of a ZNMF jet determined from a Gaussian fit, $Re_0 = 10^3$, $St_0 = 0.0072$.

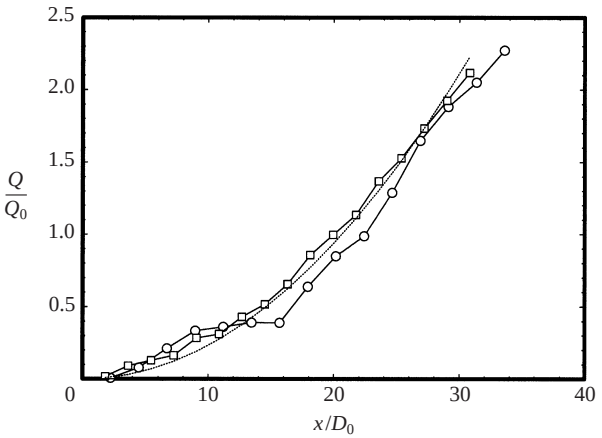

FIGURE 21. Mean, non-dimensionalized volume flow-rate, Q/Q_0. $Re_0 = 10^3$, $St_0 = 0.0072$ (□), $Re_0 = 10^4$, $St_0 = 0.0015$ (○). A parabolic curve fit is shown for comparison, (· · ·).

maximum, and back to zero again far away from the orifice. This streamwise decay of the mean centreline velocity is expected to begin where the jet becomes fully developed, at a downstream distance of approximately $25D_0$ from the orifice. This transition was expected to be closer to the orifice exit than for the equivalent continuous jet, since ZNMF jets do not have a potential core of undiminished velocity. For example, transition to self-similarity was found at $10x/h$ for rectangular ZNMF jets by Smith & Glezer (1998). The non-dimensionalized centreline velocity expressed as the ratio U_0/U_c should stretch to infinity for all the ZNMF jets at a coordinate of $x = 0$, since the mean value of the velocity across the orifice is zero. However, deviations from this would indicate a departure from a top-hat profile. Similarly, the curves for the continuous jets should intercept the axis at an approximate value of $U_0/U_c = 1$ if the exit profile is close to a top-hat. As expected from the continuity relationship, the evolution of the centreline velocity mirrors that of the radial velocity.

Figure 21 shows the volume flow rate in the near field of the ZNMF jets. The mean volume flow rate at the orifice is zero, as required. The data are non-dimensionalized by Q_0 which is calculated using $Q_0 = \pi/4D_0^2U_0^2$. Also shown for comparison is a

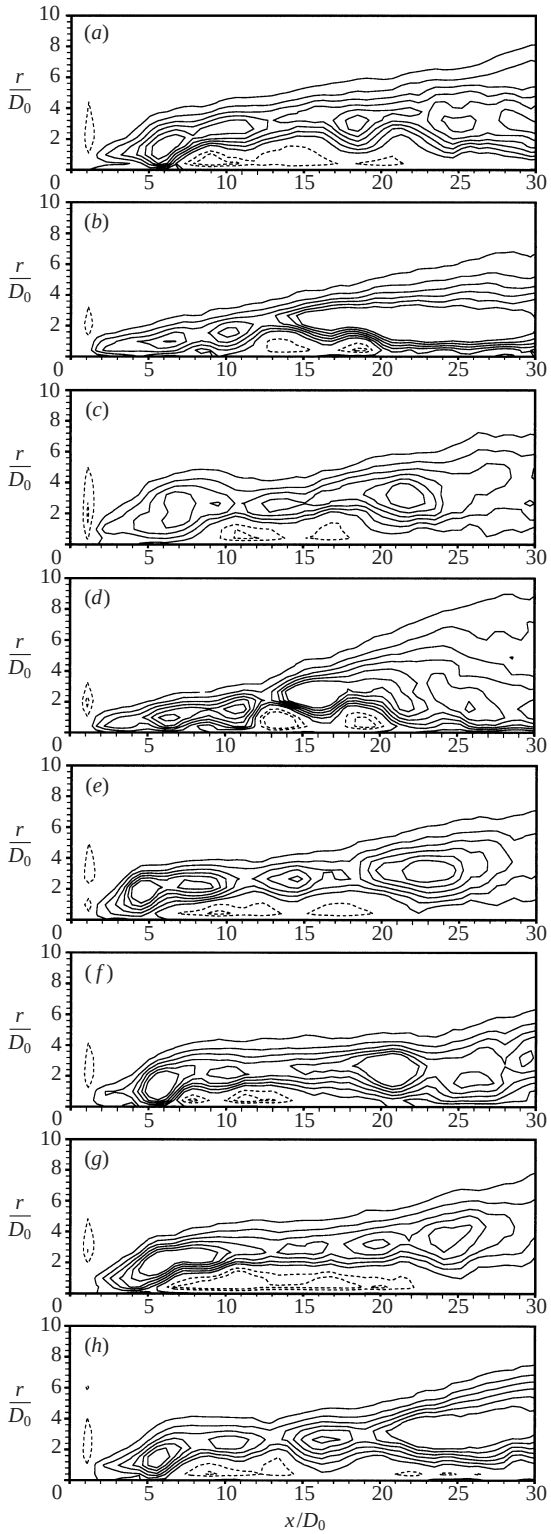

FIGURE 22. Phase-averaged, out-of-plane vorticity $\overline{\omega_\theta} D_0/2U_0$, for a ZNMF jet in increments of 5×10^{-4}, these contour levels are the same for each figure. Dashed lines represent negative values. $Re_0 = 10^3$, $St_0 = 0.0072$. Acquisitions are at times given in table 3.

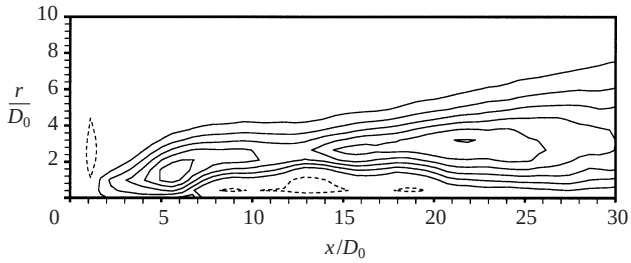

FIGURE 23. Mean, non-dimensionalized, out-of-plane vorticity $\overline{\omega_\theta} D_0/2U_0$, for a ZNMF jet, $Re_0 = 10^3$, $St_0 = 0.0072$. The vorticity is non-dimensionalized by the generation parameters: U_0, the momentum flow velocity and D_0, the orifice diameter. Displayed contour levels are values of $\overline{\omega_\theta} D_0/2U_0$ in increments of 5×10^{-4}. Dashed lines represent negative values.

parabolic relationship, $Q = C_0 x^2$. The two curves follow this relationship closely in the near field, though a linear relationship is expected when the flow is fully developed. This seems feasible beyond $x = 20D_0$.

5.6. *Phase-average measurements*

Figure 22 shows the phase-averaged, out-of-plane vorticity contours for the near field of a ZNMF jet. Each phase plot is the ensemble mean of 128 separate realizations. These data show the change in the near-field behaviour of the jet throughout the oscillation cycle. As expected the largest value of vorticity occurs at the phase when the piston is at its most forward position when $t = 0.25T_0$, which is when $\partial u_x'/\partial r$ is at a maximum. For a continuous jet the peak values of mean vorticity are expected where the mean gradient $\partial \overline{u_x}/\partial r$ is largest, i.e. close to the lip of the orifice. The phase-averaged results of the ZNMF jet show that the peak vorticity is located much further downstream, at approximately $x = 25D_0$.

A further result is that the 'wall vorticity' formed from the boundary layer on the wall behind the jet is of the same sense of rotation throughout the formation cycle. This is due to a constant radial inflow. During the forward stroke, this radial flow is entrained into the jet flow and during the piston suction stroke it is drawn into the cavity. The error in the wall vorticity measurement is also relatively high due to the small scale of the structures near the wall. Vorticity values are also compromised in the region near the orifice due to the limited spatial resolution of the measurements.

The ZNMF jet at $Re_0 = 10^3$ exhibits an interesting flow feature. Visible in every phase in figure 22 is a single vortex ring at $5D_0$ from the orifice. This is known as the 'stationary ring': it has a length scale of $4D_0$ and its existence was noted in Mallinson *et al.* (1999) and Cater & Soria (2000). Figure 23 shows the mean vorticity distribution of the eight phases at $Re_0 = 10^3$. Also visible is a change in the mean spreading rate of the jet at $13D_0$. This change occurs downstream of the stationary ring and is associated with lower values of non-dimensionalized out-of-plane vorticity at this cross-section.

5.7. *Error estimates*

Table 6 shows the calculated error estimates for the mean velocity field ε_μ, and peak vorticity measurements of the jets for the 95% confidence level as percentage values. The length scale of the velocity distribution in the self-similar region is estimated using $\eta_{1/2}$. The velocity scale is the centreline velocity, U_c. The estimate of the random error in the vorticity is calculated using equation (3.7). The radial component of velocity is one order of magnitude smaller than the x-component and therefore is

	Re_0	x/D_0	$\eta_{1/2}/D_0$	σ/μ	Δ/ℓ	ε_μ	λ_ω	$\varepsilon_{\omega_{rand}}$	$\varepsilon_{\omega_{bias}}$
Continuous	10^4	60	5.52	0.26	0.17	$\pm$1.59	2.60	$\pm$4.13	$-$1.97
ZNMF jet	10^4	60	6.42	0.35	0.15	$\pm$2.14	3.02	$\pm$6.46	$-$1.46
ZNMF jet	10^4	30	3.90	0.36	0.12	$\pm$2.21	3.89	$\pm$8.60	$-$0.88
ZNMF jet	10^3	30	3.78	0.56	0.12	$\pm$3.43	3.70	$\pm$12.70	$-$0.98

TABLE 6. Estimated errors.

much more sensitive to the measurement noise associated with PIV analysis. In fact, the magnitude of U_c at the investigated axial locations is typically 5–7 pixels while the radial component is of the order of 1 pixel.

6. Discussion

6.1. *Jet formation and structure*

The primary mechanism for the formation of round ZNMF jets is the creation of filaments with azimuthal vorticity that are generated by tangential acceleration at the orifice edge. These filaments then separate from the orifice and the evolution of all vorticity within the fluid is then determined by

$$\frac{\partial \omega_i}{\partial t} = -u_j \frac{\partial \omega_i}{\partial x_j} + \omega_j S_{ij} + \nu \frac{\partial^2 \omega_i}{\partial x_j \partial x_j}. \tag{6.1}$$

This evolution equation is valid for an incompressible fluid with homogeneous properties. The right-hand side of equation (6.1) is the summation of three distinct parts. The first term describes the convective transport of a fluid element with vorticity by the velocity field. The second part represents the amplification and rotation of the vorticity vector by the rate-of-strain field, denoted by the symmetric part of the velocity gradient tensor, S_{ij}. The final part describes the diffusion of vorticity throughout the fluid by viscosity.

The formation sequence has been examined using the phase-averaged vorticity measurements. Starting from the upstream position the piston moves forward and fluid is ejected from the cavity through the orifice. The flow separates at the sharp edges of the orifice, forming a vortex ring which begins to move away under its self-induced velocity. At low Reynolds numbers ($Re_0 < 10^3$) and low Strouhal numbers ($St_0 < 3 \times 10^{-2}$) the vortex ring has travelled sufficiently far away that it is almost unaffected by the fluid that is drawn into the cavity. As the Reynolds number is increased, for a constant Strouhal number, the rings move closer together until each loses its identity.

The ZNMF jet forms when vorticity is advected from the generator faster than it is diffused by viscosity. The results of James *et al.* (1996) suggest that a mechanism is required to remove vorticity close to the generator so that the forward and reverse motion of the oscillating boundary results in a flow field that is asymmetric in time. In the case investigated by James *et al.* (1996) the mechanism was identified as being the formation of cavitation bubbles at the surface of the membrane, which displaces fluid elements with vorticity. It was shown that a jet did not form when the cavitation bubbles were not present. It is our conjecture that if the membrane is mounted flush, there will be equal and opposite amounts of circulation at the membrane during each cycle. Without the convection of vorticity away from the orifice it is likely that

cross-annihilation and diffusion will prevent the formation of a jet. Flow visualization in the facility used for the present investigation using a membrane stretched across the orifice suggests that this is the case. In the present study, the orifice provides a sharp edge to facilitate the generation of concentrated vorticity and flow separation during the forward stroke of the piston.

George (1989) has shown that the scaling constants S_u and S_b are not universal and hence the far field can remain forever dependent on the source conditions. This has been numerically verified in the study of Boersma, Brethouwer & Nieuwstadt (1998). In a particular apparatus the far-field behaviour is determined primarily by the velocity profile and the boundary conditions. Thus, the geometry of the cylinder cavity behind the orifice will also have some effect on the bulk flow due to its influence on the exit velocity profile at the orifice. From a modelling point of view, different velocity profiles can be used to reflect different effective formation geometries.

The data reported in this paper show the mean behaviour of the jets, with a number of different time scales evident in the flow. However, a number of additional time scales need to be considered for the ZNMF jet. At $Re_0 = 10^3$, $St_0 = 0.0072$, the time scale associated with the vortex ring formation at the orifice and the time scale associated with the rotation of the primary ring may be important. From the PIV measurements, it is found that the circulation of the primary ring is approximately $0.878T_0^{-1}$. This result can be used to approximate the mean rotation period of the primary ring, which is found to be $28T_0$. This is much slower than the oscillation period of the piston. Flow visualizations of the near field suggest that the recirculation time in the tank for fluid elements that start at the orifice is larger than 10^3T_0.

Since the cavity is finite for a ZNMF jet, other time scales may be introduced into the flow from the recirculation of vortical structures within. In the same manner that the jet is formed, vortices will be generated in the cavity at the inner surface of the orifice on the suction stroke of the piston. Some degree of annihilation is expected between these vortices and the vortex rings with opposite sense produced at the piston face. Therefore, their formation cycle may change the orifice velocity profile. However, once the flow is established, the time scales are likely to be harmonics of the forcing frequency.

The asymmetry of the velocity profile during the forward and reverse stroke is evident in the numerically simulated cavity flows of Rizzetta, Visbal & Stanek (1998). A more precise comparison of ZNMF and continuous jets would be to match the initial velocity profile of the jets, but this has proved to be experimentally difficult to achieve, with the recent exception of the study by Mi, Nobes & Nathan (2001).

Wygnanski & Fiedler (1969) also obtained a different spreading rate and rate of decay in the jet far field at distances greater than $x = 50D_0$. Hussein *et al.* (1994) have attributed this difference to the loss of jet momentum due to the confinement of the jet by the boundaries of the experimental facility. It is the rapid spreading of the ZNMF jets, along with the reverse flow due to the confined nature of the experiments, that make the dimensions of the apparatus worthy of further investigation.

The lateral confinement and longitudinal confinement have opposing effects to some degree. The presence of the sidewalls of the tank narrows the streamwise velocity distribution and reduces the spread of a jet. The endwall of the tank flattens the velocity distribution and is responsible for the reverse flow surrounding a continuous jet. For a fully confined jet, the conservation of mass in each plane becomes the limiting factor. The behaviour of a round confined jet has been studied in Risso & Fabre (1997).

For the continuous jet at $x = 60D_0$ the momentum ratio given by equation (3.4) is

$M/M_0 = 0.994$. In other words, it is estimated that 99.4% of the source momentum is preserved in the jet flow. For the ZNMF jet at the same axial location the momentum ratio is equal to 0.789; since B is smaller for the ZNMF jet we can expect that it is influenced more by the reverse flow. This is a by-product of the reverse stroke.

The assumption that the jet cross-sectional area is small compared to the tank may not be appropriate in these experiments. If we assume that the cross-sectional area of the jet flow is equal to three times the half-width as suggested by Bremhorst & Hollis (1990), then the area of the jet flow is equal to half the cross-sectional area of the tank at an axial position of $250D_0$. For this reason, no data were collected beyond $100D_0$.

6.2. *Stationary vortex ring*

A conceptual model of the structure of the ZNMF jet near field at $Re_0 = 10^3$ has been developed based on the phase-averaged vorticity measurements. Close to the orifice, fluid is radially entrained throughout the oscillation cycle of the ZNMF jet generator. On the forward piston stroke this fluid is convected along with the jet flow. On the reverse stroke this fluid is drawn into the cylinder cavity. This radial flow gives rise to the boundary layer on the wall behind the jet, and thus the vorticity layer along the wall, which is similar to an annular jet.

The radial flow at the wall boundary layer is also partly responsible for the existence of the stationary ring, located $5D_0$ from the orifice. On each forward stroke the jet flow is drawn through the centre of the stationary ring and is accelerated, before expanding. Mallinson *et al.* (1999) postulated that the stationary vortex ring behaves as a venturi nozzle that accelerates and contracts the jet initially, then decelerates and diffuses the flow. After passing through the stationary ring the mean jet flow spreads more rapidly than a continuous jet. It is expected that the maximum velocity in the flow domain occurs at the centre of the stationary ring during the forward piston stroke, though in the mean the peak velocity is further downstream at an axial distance of approximately $26D_0$. After passing through the ring the jet flow entrains more fluid, then spreads and decays and finally the flow approaches a self-similar state. The presence of the stationary ring may be specific only to low Reynolds number ZNMF jets, when viscous effects are more significant.

Previous measurements with piezoelectric devices have been at higher Strouhal numbers and have not shown the presence of the stationary vortex ring. It may be that at higher Strouhal numbers the stationary ring is convected along the jet axis as seen in the low Reynolds number simulations. Thomas & Goldschmidt (1986) have found that acoustic excitations at $St_0 < 1$ significantly influence the spreading rate of continuous jets. Large increases were found for $St_0 = 0.29$, 0.42 and 0.48 with S_b up to 0.15.

This stationary ring has also been observed in the numerical simulations of Rizzetta *et al.* (1998) and Mallinson *et al.* (1999) and in the experimental study of Cater & Soria (2000). The stationary ring has a length scale of approximately $4D_0$ and a centre location that appears to oscillate between four and six orifice diameters from the orifice. This phenomenon is not evident in the vorticity field of an equivalent continuous jet.

6.3. *Jet entrainment and mixing*

In figure 18 the profile of radial velocity has an unexpected shape. The magnitude of the radial velocity increases from zero at the orifice up to a local maximum at $2D_0$. There is a minimum at $5D_0$, followed by the maximum at $15D_0$. The local

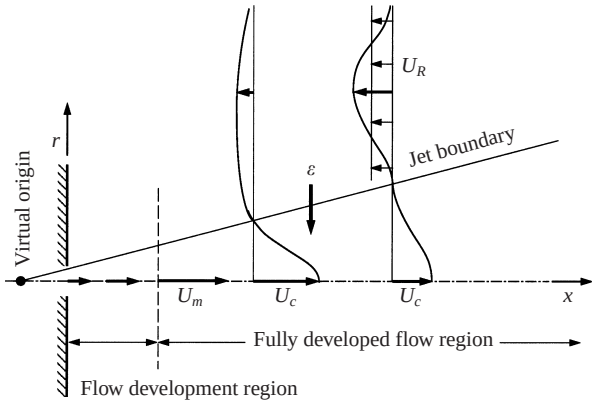

FIGURE 24. Schematic of the parameters that characterize a round ZNMF jet flow. U_m is the maximum centreline velocity of the flow. Flow is from left to right.

minimum has a streamwise position that corresponds to the location of the mean primary ring which is between $5D_0$ and $6D_0$. This result provides further evidence of the presence and location of the primary ring. When scaled by the similarity variable, measurements at radial locations greater than $25D_0$ collapse onto this curve. The resulting curve progresses from a value of zero near the wall to a peak radial velocity located between $15D_0$ and $20D_0$ and then exhibits a monotonic decay, presumably until there is interference due to the extent of the jet. A self-similar behaviour of the velocity and vorticity profiles is evident immediately downstream of this position, which corresponds to the established self-preserving behaviour observed in other continuous jet measurements. It is at this axial location that the non-dimensionalized Reynolds stresses are also at a maximum, which suggests increased mixing in this region. A schematic of the ZNMF jet flow is shown in figure 24.

It is evident from the jet half-width data shown in table 3, that transitional and turbulent ZNMF jets have a greater spread than the comparable continuous jets. This result was not initially expected since the source Reynolds numbers of the jets are similar and other published measurements contradict the present result. The central question posed by these experimental data is the nature of the mechanism responsible for the difference in the spreading behaviour.

Standard models for the formation of a vortex, such as that proposed by Gharib, Rambod & Shariff (1998), show that the starting vortex detaches from the orifice when the non-dimensional stroke length at the orifice is greater than about $4D_0$. In the present work, the non-dimensional slug length is $\gg 30$. With such a long slug at the orifice the flow field is more akin to a series of accelerating and decelerating jets. A study of the entrainment rate of a decelerating and an accelerating jet has been performed by Johari & Paduano (1997) and Zhang & Johari (1996) respectively. The approach of Johari & Paduano (1997) was to change the entrainment rate by varying the momentum of the jet. This is in contrast to the approach of Smith & Glezer (1997) who attempted to directly manipulate the shear layer using small-scale actuators. Johari & Paduano (1997) show that the deceleration phase of an unsteady jet entrains more fluid than the equivalent steady jet. Conversely, Zhang & Johari (1996) showed reduced entrainment for accelerating jets.

This behaviour is due to the relative momentum of fluid elements at each section. During the acceleration period of the jet, fluid elements upstream have more

momentum and therefore the entrainment required by continuity is less. During the deceleration, fluid elements upstream have less momentum and therefore the radial entrainment is greater. Since the mean ZNMF jet flow decelerates with axial coordinate more rapidly than the continuous jet, the total radial entrainment over a period is greater.

Liepmann & Gharib (1992) have demonstrated how streamwise vortex pairs form between the predominant vortex rings of the continuous jet. They further highlighted the importance of these streamwise vortex pairs in the entrainment process of ambient fluid. These structures have also been observed in the wake of turbulent separated vortex rings and therefore the presence of streamwise vortices in the wake of each pulse may also act to increase the mixing of the ZNMF jets at low Strouhal numbers.

In summary, the reason that ZNMF jets spread differently throughout the domain is due to structural differences in the near field. Although, the shape of the mean velocity profiles is similar to a continuous jet in the far field, the mean streamwise gradients are different. This important difference persists and propagates through the nonlinear terms in the equations of motion, specifically through the term $u_x \partial u_x / \partial x$. In other words, it is possible that at some point in the flow an 'equivalent' continuous jet and a ZNMF jet have the same momentum and velocity profile, but the streamwise velocity gradients are different due to the increased radial inflow in the near field. This leads to the non-universality of constants in similarity solutions for turbulent jets across different velocity profiles, as well as the source Strouhal number dependence of the jet statistics. In the ZNMF jets, the velocity gradients are also a function of the actuator phase as shown in the phase-averaged vorticity profiles.

7. Conclusions

This study demonstrates that the round turbulent ZNMF jet has a similar cross-stream velocity distribution to that of a conventional continuous jet but with a larger spreading rate and decay constant. A stationary primary ring has been identified in the near field of the ZNMF jet that remains throughout the ZNMF jet cycle at $Re_0 = 10^3$, $St_0 = 0.007$. This structure has a length scale which is approximately four times the jet orifice diameter. It is suggested that this large-scale structure is responsible for a peak in the jet radial entrainment at a position approximately fifteen diameters downstream of the orifice. Structural differences in the near field of ZNMF jets compared to continuous jets are responsible for different streamwise velocity gradients and, hence, the different spreading and different velocity decay behaviour that is observed.

The financial support of the ARC to undertake this research is gratefully acknowledged.

REFERENCES

Boersma, B. J., Brethouwer, G. & Nieuwstadt, F. T. M. 1998 A numerical investigation on the effect of the inflow conditions on the self-similar region of a round jet. *Phys. Fluids* **10**, 899–909.

Bremhorst, K. & Hollis, P. 1990 Velocity field of an axisymmetric pulsed, subsonic air jet. *AIAA J.* **28**, 2043–2049.

Cater, J. E. 2002 Experimental investigation of the turbulent axisymmetric jet. PhD thesis, Monash University, Melbourne, Australia.

Cater, J., Bertillino, F. & Soria, J. 1999 Investigation of the far field of axisymmetric zero-net-mass

flux jets using cross-correlation PIV. In *Proc. Second Australian Conf. on Laser Diagnostics in Fluid Mechanics and Combustion* (ed. J. Soria & D. Honnery), pp. 144–149. Monash University, Melbourne, Australia.

Cater, J., von Ellenrieder, K. & Soria, J. 2001 Phase-averaged PIV measurements of turbulent ZNMF jets. In *5th World Conf. on Experimental Heat Transfer, Fluid Mechanics and Thermodynamics, Thessaloniki, Greece* (ed. G. P. Gelata, P. Dimarco, A. Goulas & A. Mariani). Edizioni ETS, Pisa.

Cater, J. & Soria, J. 2000 Comparisons between axi-symmetric zero-net-mass flux jets and continuous jets. In *7th Heat and Mass Transfer Conf. Australasia* (ed. G. Brassington & J. Patterson), pp. 75–80. Townsville, Australia: Chalkface Press.

Chang, Y. K. & Vakili, A. D. 1995 Dynamics of vortex rings in crossflow. *Phys. Fluids* **7**, 1583–1597.

Coe, D., Allen, M., Trautman, M. & Glezer, A. 1994 Micromachined jets for manipulation of macro flows. *Technical Digest, Solid-State Sensor and Actuator Workshop (Hilton Head '94), Hilton Head Island, SC*, June 13–16, pp. 243–247, Transducer Research Foundation, OH, USA.

Davis, S. A. & Glezer, A. 1999 Mixing control of fuel jets using synthetic jet technology: velocity field measurements. *AIAA Paper* 99-0447.

von Ellenrieder, K., Kostas, J. & Soria, J. 2001 Measurements of a wall-bounded turbulent, separated flow using HPIV. *J. Turbulence* **2**, 1–15.

Eroglu, A. & Breidenthal, R. E. 2001 Structure, penetration, and mixing of pulsed jets in crossflow. *AIAA J.* **39**, 417–423.

Fouras, A. & Soria, J. 1998 Accuracy of out-of-plane vorticity measurements using in-plane velocity vector field data. *Exps. Fluids* **25**, 409–430.

George, W. K. 1989 The self-preservation of turbulent flows and its relation to initial and coherent structures. In *Advances in Turbulence* (ed. W. K. George & R. E. A. Arndt), pp. 37–72. Hemisphere.

George, W. K. & Hussein, H. J. 1991 Locally axisymmetric turbulence. *J. Fluid Mech.* **233**, 1–23.

Gharib, M., Rambod, E. & Shariff, K. 1998 A universal time scale for vortex ring formation. *J. Fluid Mech.* **360**, 121–140.

Hermanson, J. C., Wahba, A. & Johari, H. 1998 Duty cycle effects on penetration of fully modulated, turbulent jets in crossflow. *AIAA J.* **36**, 1935–1937.

Hussein, H. J., Capp, S. P. & George, W. K. 1994 Velocity measurements in a high-Reynolds number, momentum conserving, axisymmetric, turbulent jet. *J. Fluid Mech.* **258**, 31–75.

James, R. D., Jacobs, J. W. & Glezer, A. 1996 A round turbulent jet produced by an oscillating diaphragm. *Phys. Fluids* **8**, 2484–2495.

Johari, H., Pacheco-Tougas, M. & Hermanson, J. C. 1999 Penetration and mixing of fully modulated turbulent jets in crossflow. *AIAA J.* **37**, 842–850.

Johari, H. & Paduano, R. 1997 Dilution and mixing in an unsteady jet. *Exps. Fluids* **23**, 272–280.

Kral, L. D., Donovan, J. F., Cain, A. B. & Cary, A. W. 1997 Numerical simulation of synthetic jet actuators. In *4th AIAA Shear Flow Control Conference, June 29–July 2, 1997, Snowmass Village, CO*. AIAA.

Liepmann, D. & Gharib, M. 1992 The role of streamwise vorticity in the near-field entrainment of round jets. *J. Fluid Mech.* **245**, 643.

Lighthill, S. J. 1978 Acoustic streaming. *J. Sound Vib.* **613**, 391–418.

Mallinson, S. G., Hong, G. & Reizes, J. A. 1999 Some characteristics of synthetic jets. *AIAA Paper* 99-3651, pp. 1–10.

Mi, J., Nobes, D. S. & Nathan, G. J. 2001 Influence of jet exit conditions on the passive scalar field of an axisymmetric free jet. *J. Fluid Mech.* **432**, 91–125.

Morton, B., Taylor, G. I. & Turner, J. S. 1956 Turbulent gravitational convection from maintained and instantaneous sources. *Proc. R. Soc. Lond.* **234**, 1–23.

Panchapkesan, N. R. & Lumley, J. L. 1993 Turbulence measurements in axisymmetric jets of air helium. Part 1. Air jet. *J. Fluid Mech.* **246**, 197–223.

Panchapakesan, N. & Soria, J. 1999 Separation control using surface oscillations – some preliminary results. In *Proc. Second Australian Conf. on Laser Diagnostics in Fluid Mechanics and Combustion* (ed. J. Soria & D. Honnery), pp. 105–106. Monash University, Melbourne, Australia.

Piquet, J. 1999 *Turbulent Flows: Models and Physics*. Springer.

Rajaratnam, N. 1976 *Turbulent Jets*. Elsevier.

Ricou, F. P. & Spalding, D. B. 1961 Measurements of entrainment by axisymmetric jets. *J. Fluid Mech.* **11**, 21–32.

Risso, F. & Fabre, J. 1997 Diffusive turbulence in a confined jet experiment. *J. Fluid Mech.* **337**, 233–261.

Rizzetta, D., Visbal, M. & Stanek, M. 1998 Numerical investigation of synthetic jet flowfields. In *29th AIAA Fluid Dynamics Conference, June 15–18 1998, Albuquerque, NM*. AIAA.

Rizzetta, D., Visbal, M. & Stanek, M. 1999 Numerical investigation of synthetic jet flowfields. *AIAA J.* **37**, 919–927.

Smith, B. L. & Glezer, A. 1997 Vectoring and small-scale motions effected in free shear flows using synthetic jet actuators. *AIAA Paper* 97-0213.

Smith, B. L. & Glezer, A. 1998 The formation and evolution of synthetic jets. *Phys. Fluids* **10**, 2281–2297.

Soria, J. 1996*a* An adaptive cross-correlation digital PIV technique for unsteady flow investigations. In *Proc. 1st Australian Conf. on Laser Diagnostics in Fluid Mechanics and Combustion* (ed. A. Masri & D. Honnery), pp. 29–48. University of Sydney, Sydney, NSW, Australia.

Soria, J. 1996*b* An investigation of the near wake of a circular cylinder using a video-based digital cross-correlation particle image velocimetry technique. *Expl Therm. Fluid Sci.* **12**, 221–233.

Soria, J. 1998 Multigrid approach to cross-correlation digital PIV and HPIV analysis. In *Proc. 13th Australasian Fluid Mechanics Conf.* (ed. M. C. Thomson & K. Hourigan). Monash University, Melbourne, Australia.

Soria, J., Cater, J. & Kostas, J. 1999 High resolution multigrid cross-correlation digital PIV measurements of a turbulent starting jet using half frame image shift film recording. *Opt. Las. Technol.* **31**, 3–12.

Tennekes, H. & Lumley, J. 1972 *A First Course in Turbulence*. The MIT Press.

Thomas, F. O. & Goldschmidt, V. W. 1986 Structural characteristics of a developing turbulent planar jet. *J. Fluid Mech.* **163**, 227–256.

Vermeulen, P. J., Chin, C.-F. & Yu, W. K. 1990 Mixing of an acoustically pulsed air jet with a confined crossflow. *J. Propulsion* **6**, 777–783.

Widnall, S. E. & Tsai, C. 1977 The instability of a thin vortex ring of constant vorticity. *Proc. R. Soc. Lond.* **A 267**, 273–305.

Wu, J. M., Vakili, A. D. & Yu, F. M. 1988 Investigation of the interacting flow of nonsymmetric jets in crossflow. *AIAA J.* **26**, 940–947.

Wygnanski, I. & Fiedler, H. 1969 Some measurements in the self-preserving jet. *Phys. Fluids* **38**, 577–612.

Zhang, Q. & Johari, H. 1996 Effects of acceleration on turbulent jets. *Phys. Fluids* **8**, 2185–2195.